FABRICATION AND CHARACTERIZATION OF POROUS 316L STAINLESS STEEL USING SELECTIVE LASER MELTING TECHNIQUE FOR BIOMEDICAL APPLICATIONS

A Thesis

by

OGHOGHO CYNTHIA OMORAGBON

Submitted to the Office of Graduate and Professional Studies of
Texas A&M University
in partial fulfillment of the requirements for the degree of

MASTER OF SCIENCE

Chair of Committee,	Hong Liang
Co-Chair of Committee,	Chao Ma
Committee Member,	Michael B. Pate
Head of Department,	Andreas A. Polycarpou

August 2018

Major Subject: Mechanical Engineering

ABSTRACT

Porous metals play essential roles in lowering the value of elastic modulus, achieving a modulus like that of the human body. Solid freeform fabrication has the potential to overcome the limitations of traditional manufacturing methods with controlled internal pore architecture. The use of 3D printing has been solely focused on polymer materials with limited investigations on producing porous metallic parts, such as implants. This research studies the influence of 3D printing on the pore architecture and its impact on cell growth. Selective laser melting (SLM), an additive manufacturing process, was used to fabricate 316L stainless steel porous structures. The stainless steel was selected for this research as a model system due to its known properties.

Four cubic models of 15×15×4 mm^3 were designed using Autodesk inventor with interconnected pore sizes of 0.4 mm, 0.6 mm, 0.8 mm, and 1.0 mm. The CAD files were converted to STL models and then extracted into QuantAM software, which produces printing instructions for the Renishaw AM400 SLM machine. The results show that 316L stainless steel porous structures with fully interconnected pores were successfully fabricated using the SLM process, with a mean pore size reduction of 0.220 mm for all samples.

The samples were subjected to an accelerated corrosion test for 336 hours using the salt spray chamber. 5 % wt. of NaCl formed part of the composition of the corrosive media, and by comparing the corrosion rates and weight loss of the interconnected structures, the samples experienced an insignificant percentage weight loss and an average corrosion rate of 3.0 mpy.

The cell culture experiment reveals the cell growth viability of all samples of the selective-laser-melted 316L stainless steel structures seeded with *Pseudomonas aeruginosa* cells, for pore

sizes ranging between 0.182 mm to 0.783 mm. The 0.783 mm porous structure with the highest porosity of 61.2% was most conducive to biofilm formation, allowing cell ingrowth into the pores.

DEDICATION

I dedicate this thesis to God, my parents, Charles Omoragbon and Susan Omoragbon, my significant other, extended family members, professors, mentors, mentees, and all who have supported me through my graduate program, for their love, fountain of wisdom, experience, advice, prayers, mentorship, patience, and all-round support. These have yielded much fruit in me and have made me better than yesterday, in every ramification of my life, with enhanced knowledge, skills, and a well of vast experience. I am prepared to contribute my quota of technical impact to the global world.

ACKNOWLEDGEMENTS

First, I render thanks to God for guiding me through my graduate program. He has been my ultimate source that never runs dry.

Thanks to my parents and the Aremu family for being the best parents in the world and to my siblings for their greatest support.

I would like to express my sincerest gratefulness to my chair, Professor Hong Liang, my co-chair, Dr. Chao Ma, and my committee member, Dr. Michael Pate, for their guidance and support throughout my research program. My research skills have significantly improved.

Furthermore, I would like to acknowledge Boluwarin Aremu, for his love, patience, wisdom, and assistance, for motivating me to greatness.

My gratitude goes to the surface science group and Dr. Ma's research group, for the contribution to this work, in particular, Yuan Yue, Lian Ma, John Reis, Ming Li, and Carlos Elizondo.

Special thanks go to Professor Alan Palazzolo, for giving me my first job in the US, in the Vibrations Controls and Electromechanical Lab. I learned the art of making great electromagnetic motor coils, among other great experiences. Working with Thomas Erwin, Segun Tytler and Stephen Farris, was one of the memorable experiences at the Lab.

My heartfelt thanks go to Ms. Sandy Havens, for her beautiful personality, for being resourceful and always ready to help, with respect to my success in graduate school, even before my arrival to the US, to commence my graduate program.

Additionally, I would like to recognize the essential guidance of my supervisor Satya-Kal Dukka, for being a great leader during the course of my Co-op program with Cummins Inc., in

realizing my potentials, assigning job responsibilities to me and offering full support, all of which has developed my technical skills, background, knowledge, and experience in manufacturing engineering.

Great thanks also go to the best friends in the world: Joseph Oh, Gloria Oh, Edobor Edeoba, Ayomikun Adeniran, Uche Adeniran, Ore Atobatele, Diane Uwacu, Mary-Echi Ali, Ehikowoicho Idoko, Tracy Obi, Chukwuemeka Obi, Moffi Adetayo, Ayodeji Adeniran, Tolu Babarinde, Dean Mbabazi, Amanda Parkman, Shannon Shahkarami, Charlie Brent, Chelsea Lunsford, Vaibhav Rungta, Shefali Rana, Joshua Ebin, Jamie Evans, Karl Evans, Judy Mcdaniel, Tony Mcdaniel, Ashley Mcdaniel, Yetunde Ewuola, Lawrence Bukenya, Jainaba Faal, Tolu Oke, Queen Oke, Jacqueline Antwi-Danso, James Ishaku, Nelie Kouamou, Moyosore Ajeigbe, Obi Michael, Tosin Obadara, John Ogaga, Femi Olorede, Yash Parikh, Miguel Talavera, Aderinsola Oduntan, Makanjuola Adara, Cesar Pelli, Vaidehi Tawari, Xiomeng Tong, Rakiya Adamu, Elias Adanu, Rev.d Robert, Larry Joiner, Rebecca Preston, Christiana Ikhana, Mykala Madson, all my friends I have not mentioned here, colleagues, faculty, and staff for enhancing my time spent at Texas A&M University.

I would also like to appreciate the Mechanical Engineering Female Engineering Graduates Association and National Society of Black Engineers for the opportunity to express my ideas to the team.

Finally, my sincere appreciation to Mr. and Mrs. Omoruyi and Mr. and Mrs. Agho for their assistance towards the advancement of my career.

.

CONTRIBUTORS AND FUNDING SOURCES

Professor Hong Liang and Dr. Michael Pate, of the Department of Mechanical Engineering, and Dr. Chao Ma, of the Department of Engineering Technology and Industrial Distribution, and forming members of my thesis committee, supervised this work

Carlos Elizondo helped in the design of the porous structures. Lian Ma trained me on Scanning Electron Microscope (SEM) imaging of the 3D printed structures. The Department of Mechanical Engineering at Texas A&M University provided the SEM facility and salt spray chamber for evaluating corrosion rate and weight loss of specimens utilized in this study. John Reis offered training and assisted in carrying out the salt spray accelerated corrosion test. David Malawey helped in 3D printing the porous structures using the Renishaw AM400 selective laser melting (SLM) machine and provided a thorough explanation on the working principles of the SLM Technique. Dr. Preeti Sule of Dr. Jeff Cirillo's group and Yuan Yue helped in the cell culture experiment and SEM characterization of the cell-seeded structures. Ming Li also helped with the SEM imaging of the smallest pore size structure for the melt pool analysis. Dr. Carlos Sanchez assisted with the white light interferometry imaging of all the samples.

The Department of Engineering Technology and Industrial Distribution at Texas A&M University supported my graduate program during the spring semester, via a graduate teaching assistantship.

NOMENCLATURE

AM	Additive Manufacturing
SLM	Selective Laser Melting
EBM	Electron Beam Melting
SLS	Selective Laser Sintering
FDM	Fused Deposition Modeling
CAD	Computer Aided Design
RP	Rapid Prototyping
SFF	Solid Freeform Fabrication
ECM	Extracellular Matrix
LOM	Laminated Object Manufacturing
LENS	Laser Engineered Net Shaping
STL	Standard Triangle Language
MPY	Mils Penetration per Year
LED	Linear Energy Density
VED	Volumetric Energy Density
SLA	Stereolithography Apparatus
TEC	Tissue-Engineering Construct
PC	Polycarbonate
ABS	Acrylonitrile Butadiene Styrene
PPSF	Polyphenylsulfone
YAG	Yttrium-Aluminium-Garnet

HA	Hydroxyapatite
PLLA	Poly-l-lactic Acid
PGA	Polyglycolic Acid
PLGA	Poly-dl-Lactic-co-glycolic acid
CFU	Colony-Forming Unit
CAD	Computer Aided Design
RVC	Reticulated Vitreous Carbon
ASA	Acrylonitrile Styrene Acrylate

TABLE OF CONTENTS

Page

LIST OF FIGURES

Page

LIST OF TABLES

Page

CHAPTER I

INTRODUCTION AND LITERATURE REVIEW

Tissue engineering provides promising grounds for additive manufacturing in fabricating spinal fixation devices, pins, wires, fracture plates, screws, and dental implants. Additive manufacturing techniques possess tremendous advantages over traditional manufacturing technologies in producing a wide variety of functional end-use components [3], complex geometry and internal channel networks that mimic the bone structures, and enhanced materials properties and performance by varying processing parameters [4]. Revised surgery is minimized, as customized implants can be developed and optimized for patients using their analytical information from medical CT scanners.

The discrepancy between Young's modulus of the human bone and that of solid metals poses a major setback for metallic implants in the orthopedic field. The use of porous metals has been found to play a significant role in lowering the value of elastic modulus to achieve a modulus like that of the human body [5]. Solid freeform fabrication has the potential to overcome the limitations of traditional manufacturing methods with controlled internal structure.

The use of 3D printing has been limited to polymers with limited investigations on producing porous metallic parts such as implants [6]. Metals possess high fracture strength, high fatigue strength, and low weight to high strength ratio, which makes them suitable for load-bearing applications. Therefore, this research investigates the effect of 3D printing on the pore architecture and cell growth viability of the 316L stainless steel printed structures.

This chapter gives a fundamental background of this research to aid comprehension of fundamental concepts expatiated in subsequent chapters.

1.1 The Significance of Additive Manufacturing

Additive Manufacturing (AM), popularly known as 3D printing [7] or direct digital manufacturing, involves manufacturing end-use components by the addition of powdered materials in a layered form from a 3D computer CAD digital model [4]. Although rapid mass production of parts is unlikely to be achieved via AM technique, its significance is evident in applications that require the fabrication of components that are difficult to manufacture using traditional manufacturing methods.

With cost and lead time associated with tooling, inventory, labor, payload, assembly of multiple parts, and maintenance cost eliminated, many industries are welcoming AM methods. The aerospace industry, for example, utilizes this technique to produce housings, plastic enclosures, and other nonstructural parts [8]. These parts are manufactured in one piece and are tested, inspected, and shipped in a shorter time interval. Over the past 15 years, Boeing and its contractors have produced highly complex air ducting for F-18 with laser sintering. And in 2017, Reuters reported that additive manufactured titanium parts will be used in the fabrication of the Boeing 787 Dreamliner Jet airliner, using a direct digital manufacturing technique called rapid plasma deposition, by melting titanium wire in an inert environment of argon gas to make parts [9]. The raw material cost and energy usage are said to be reduced by this process, as when compared to conventional forging and machining, which results in a cheaper build cost for each jet [10]. Companies are advancing towards certifying metals, like titanium and cobalt-chrome, for AM techniques, with the primary aim of utilizing SLM and EBM processes, to fabricate complex and expensive parts [8].

The medical industry is another growing field for AM application, as metallic implants, 3D scaffolds, etc. can be produced using AM methods. Examples include fracture plates and hip

sockets, which require the use of Ti6Al4V alloy for implantation on patients, as well as gold and CoCr coping used in the dental industry as a primary structure in crowns and bridges, produced using the EBM and SLM techniques. Dental labs are looking for new ways, such as AM processes, to increase profitability and efficiency in the process of manufacturing crowns and bridges to ensure their timely completion and availability to the dentist, as the revenue for crowns and bridges in the U.S. is approximately 8.5 billion dollars every year. Research shows that 380 CoCr copings can be produced using an EOSINT M 270 machine (a DDM technique) in 20 hrs; on the other hand, it would take a dental technician to produce 8-10 crowns in one workday using traditional manual manufacturing methods [8].

Research on the benefits of additive manufacturing in producing long-term usable components [11] will continue to be explored as people and organizations comprehend its possibilities and limitations. The current challenges faced within the field of additive manufacturing spur the development of AM methods, subsystems, materials, and product design [8]. With the advancement of 3D printing, designers are trained to specialize in designing structures for improved performance, instead of fixing the restraint of traditional processes such as machining, casting, etc. [12].

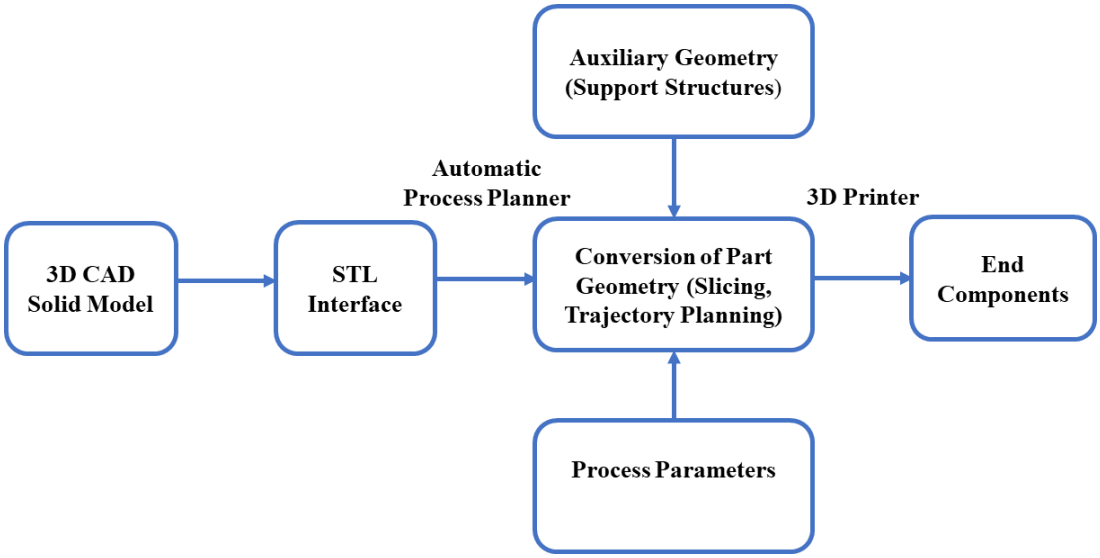

Figure 1. Solid freeform fabrication process from design to manufacturing.

This research investigates the effect of 3D printing on the pore architecture and biocompatibility of the printed structures. This research will guide future research on controlling the parameters for the printing process and architecture of the pore design to achieve optimal pore architecture for cell growth viability.

1.2 Setbacks of Additive Manufacturing

Despite the geometrical flexibility of direct metal manufacturing techniques, the size of the components is process dependent. Medium sized parts can be produced using current AM methods such as SLS, SLA, and FDM. However, these techniques are limited to the fabrication of large parts due to their performance, availability of large commercial equipment, and cost considerations [11]. Lowering RP equipment cost is becoming a crucial goal for most U.S. equipment makers. Some manufacturers set the prices of their machines based on the components and assembly cost [13] or tend to position themselves as high-cost premium manufacturers [1] to encourage

favourable perception of high value to buyers. Low volume production is also associated with AM technologies, and thereby increases the cost of attaining economies of scale via batch production [14].

Support structures are required to be constructed underneath the parts to hold parts connected to another and to support overhanging portions that are weak during the layer formation. This implementation of support structures requires an additional amount of time and material, and these structures may be difficult to remove without damaging the desired parts or may sometimes require manual removal for some AM methods [15]. Loose unsolidified powdered materials during AM, may block the pores on porous structures, impeding their performance, for example, in porous implants.

Process performance also possesses a major concern, with respect to the quality, printing accuracy, and surface finish of the AM fabricated components [11]. Most 3D printed surfaces are rough in nature, depending on the layer thickness, orientation of work piece, and surface inclination [11] requiring post-processing, like surface heat treatment. The development of software and procedures, both for the front and back end process of AM technique, to optimize the control, repeatability, and data quality of parts is essential [8]. According to research studies, stereolithography is mostly preferred in places like Japan, due to its higher accuracy capabilities, as when compared to the laser sintering techniques.

The speed of building parts is open for improvements, in the automatic design of structural supports, eliminating the need to manually design supports through the software that generates instruction for the AM machines like QuantAM for Renishaw. It takes a longer time for components to be produced [1].

1.3 Scaffold Requirements

In tissue engineering, scaffolds are integrated with live cells or bioactive factors to produce tissue-engineering constructs (TEC) for tissue regeneration and repair [16]. Medical treatment of bone or cartilage defects from fractures, diseases, tumors, infections, trauma, or abnormal skeletal defect development [17] that cannot be repaired require bone grafts or tissue transplantation, which can be obtained in the form of an allograft or autograft for the restoration of the skeleton function.

With the evolution of synthetic bone replacement scaffolds, the problem of donor site scarcity, disease transfer, and immune rejection is eliminated [18]. An approach is obtained when cells derived from the human tissues are seeded on 3D scaffolds to stimulate, direct and enhance tissue regeneration into the structures, when delivered in the patient's body [19, 20]. Scaffolds help support cell colonization, migration, growth, and differentiation [16]. The construction of the scaffold controls the formation of the new bone and cartilage [20]. To an achieve an optimized scaffold, the structures should be highly porous and possess a high degree of pore interconnectivity to support cell growth and the transfer of nutrients and body waste [21, 22]. They should also be biocompatible and bioresorbable, with the ability to degrade and resorb slowly like that of the desired cell [20]. Figure 2 shows the production technique for engineered tissues utilizing biomaterial scaffolds, designed with biological requirements [23]. A combination of both known and unknown, 3D space and temporal gradient factors determines how tissues can be developed with acceleration and remodeled. The biomimetic technique is used to design scaffolds that enhance structural, mechanical support for cell attachment and tissue regeneration [23].

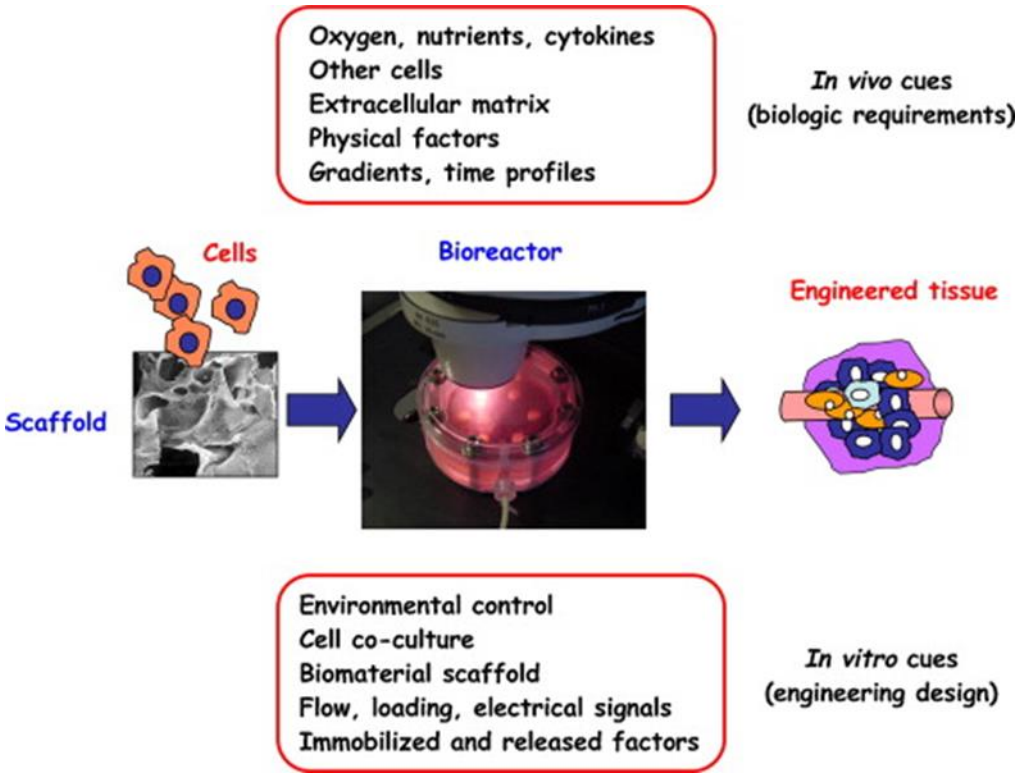

Figure 2. Developmental biology and tissue engineering. [23] Reprinted with permission.

Biomimetic also combines the design of biomaterial scaffolds with the design of bioreactors in providing the environmental control, metabolites, exchange of nutrients, etc., to mimic the neighborhood of the cells in animals. The design of tissue engineering systems is guided by the biological requirements, resulting to optimized models [23].

The 3D scaffold should not result in an adverse inflammatory effect on the patient. Cell attachment, proliferation, and differentiation are essential in improving the functions of scaffolds [20]. The mechanical properties such as the strength, stiffness, etc. should be like that of the human bone/tissue at the site of implantation.

1.4 Problems Associated with Current Implants

The principal goal of designing scaffolds for tissue regeneration is to repeat the ECM growth process in a short-term organized structure. The control of all forms of desired cell response, in the form of cell guidance, attachment, movement, proliferation, and differentiation, both at the cellular and tissue level should be attainable in an ideal scaffold [24].

Materials currently tested as scaffolds for tissue engineering can be grouped into natural, synthetic, and hybrid materials based on their origins [25]. Polymeric materials from natural origins have numerous advantages, which include important biological reaction, the formation of cellular-like environment structures, and biodegradability. Today, synthetic materials are widely considered for biomedical applications over the natural materials, due to their advantages in reducing the risk of viral infection [25], material scarcity, and antigenicity, and their material properties can be controlled to enhance tissue/cell performance. Synthetic materials are still limited in their use as tissue scaffold, because of their reduced biocompatibility limit. The creation of hybrid materials occurs through seeding cells chemically into synthetic structures with the tendency to promote direct biological interaction with the cells [24]. This technique still requires refinement as factors guiding cell response on 3D scaffold materials need to be investigated and outlined.

Implants, fabricated for the ingrowth of bones or cells into the scaffolds, are dependent on the mechanical strength and biological anchorage of the surrounding host bone tissue to the scaffolds and therefore may also experience stability issues [26]. Implant loosening occurs due to stress shielding of the bone, resulting from Young's moduli dissimilarity between the host bone and biomaterial. Implant loosening resulting from the bone being insufficiently loaded, becoming stress shielded, and eventually resulting in bone loss, may hinder the scaffold's performance in

promoting cell ingrowth. Bone resorption from stress shielding poses problems for revised surgery [5] . Current research focus lies in achieving Young's moduli similar to the human bone.

1.5 Significance of Porous Metals

To achieve a match between Young's moduli of the host bone and that of the biomaterial, a balance between stiffness and strength, the implant should possess high strength for load bearing applications [5]. Researchers have revealed that the use of porous materials is effective in lowering elastic modulus and stiffness values, to achieve a modulus similar to that of the human body based on the total bulk porosity [5]. Porous materials have been investigated and proven to be potential candidates for achieving bone ingrowth on their surfaces. Open pore materials provide high fixation points that promote skeletal fixation on the interface.

Research has proven that porous metals help tissues grow and improve the Osseointegration of implants to the bone host. Three-dimensional porous materials that form part of the 3D scaffolds [21] help to control, support, and trigger mammalian cells [22] and bone ingrowth as a function of pore interconnectivity and enhance functionality [21].

Researchers have focused on porous metals for orthopedic application requiring load bearing because of their superior fracture and fatigue resistance and use in ultra-lightweight metallic structures [28]. Porous ceramics cannot be utilized for loadbearing applications due to their brittleness, with poor mechanical properties in relation to the human bone. Polymer chains are also not capable of withstanding mechanical forces [5].

Also, metal foams are being used today in furniture design for light-weight construction structures, energy absorption, filtration applications, and other thermal management applications [29, 30]. The material's multifunctional qualities stem from its low density, and the relationship between it's mechanical, electrical, thermal, and sound properties [29].

1.5.1 Types of Porous Structures

1.5.1.1 Open Cell Porous Structures

Open cell structures promote the ingrowth of cells through the interconnectivity of individual network of cells. Porous open cell structures are significant in applications such as filtration, sound or energy absorption, heat or mass exchange, separation, etc. [31]. Porous implants also allow the fixation of newly grown cells/ tissue to the scaffolds, anchoring it into position. Higher porosity can be achieved in open cell porous structures. Metallic open foams possess more extensive applications in functional structures, such as in the medical field to promote bone ingrowth [31].

1.5.1.2 Closed Cell Porous Structures

In closed cell structures, each cell is enveloped by a film of metal or thin wall, with a variation of physical and internal properties dependent on the processing parameter of the manufacturing technique [5]. Closed cell porous structures have higher elastic moduli, higher strength, higher fatigue resistance and higher impact resistance (toughness). This type of porous structure does not facilitate cell growth due to the poor or non-interconnectivity of its pores. The advantages of closed pores can be viewed in the area of the reduction of stiffness to correlate with the mechanical properties of the bone and ultimately reducing stress shielding.

1.5.2 Traditional Fabrication Techniques for Porous Structures

Foams are generally produced through various technique, which can be categorized into four groups; vapor deposition, metal sputtering, melt, powder metallurgy. Two mechanisms, self-formation or pre-design, are generally used to create porosity irrespective of foam production method [29].

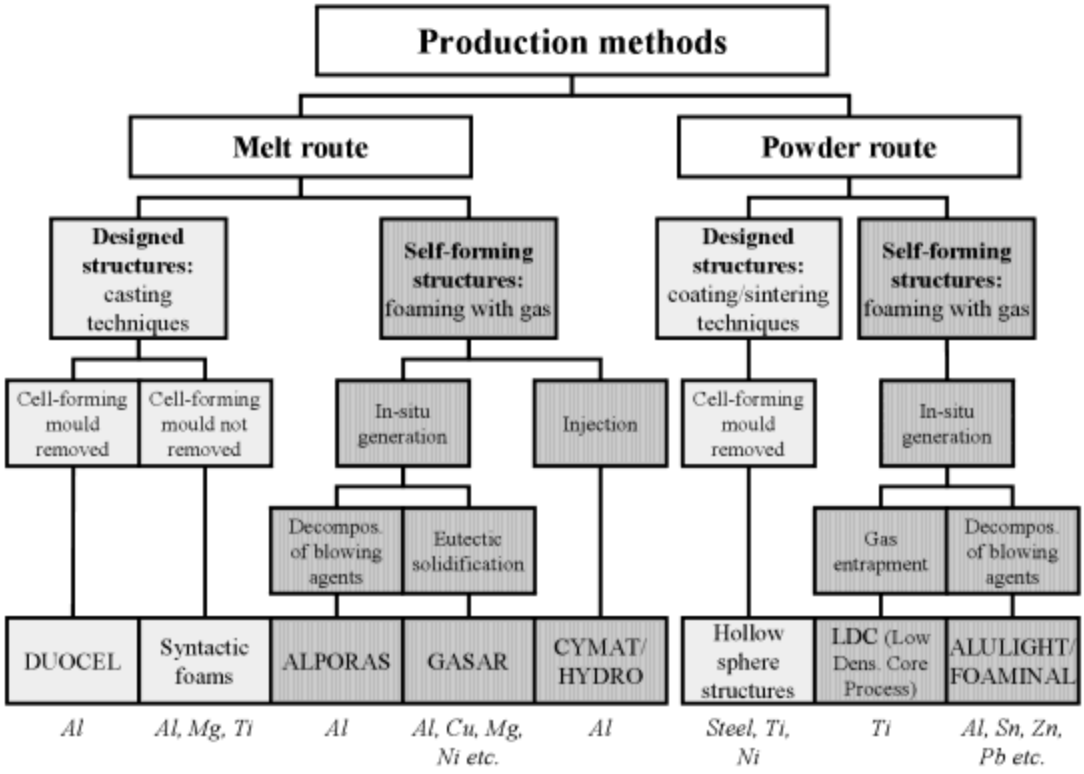

Figure 3. Processing techniques to produce metallic foams. [29] Reprinted with permission.

1.5.2.1 Self-Formation

Self – forming process is utilized to create pores based on physical principles. An example is the addition of gas forming elements to a liquid metal or the injection of gas through a melt to generate gas bubbles [5]. The cell walls are usually stabilized using additives such as SiC- or Al2O3 particles to increase the low melt viscosity, decrease the surface energy and stabilize the bubbles of pure metals.

1.5.2.2 Pre-design

The pore cell structures are usually formed by using cell forming molds, in which sphere-like particles are enclosed within the molten metal. The particles may be solid or hollow particles. If they are solid, they must be removed to create holes in the metal foam product [32]. The

advantages this has over self-forming foams are; pore architecture and other cell structure properties can be pre-selected based on the size of the powder, resulting in improved and more uniform mechanical properties [31].

1.5.2.3 Plasma Spraying

Plasma spraying is utilized to create porous structures. It is a form of thermal spraying technique in which an electric dc arc or radio frequency is produced amid water-cooled electrodes. The electric dc arc serves as the heat source. Plasma jet is formed by heating gases and partially ionizing them via dc arc or radio frequency to very high temperatures of 20,000 $^{\circ}$C. Plasma and plasma jets are also referred to as radio frequency (RF) and direct current (DC) arc respectively. Powdered particles are inserted into the plasma or plasma jet with a carrier gas, which is then accelerated to high speed, subjected to full or partial melting, before solidification on the substrate [33]. The degree of porosity can be controlled by modifying the parameters of the process [5]. The drawback associated with these techniques involves porosity irregularity, limited pore interconnectivity, high product cost, and the introduction of impurity phases in the porous structures [5].

1.5.2.4 Space Holder Method

This production process produces a higher degree of porosity and uniform pore structures. Space holders and metallic powdered material are blended and condensed to create a green body. The green body pellets undergo a low-temperature heat treatment procedure to remove the space holders, resulting in the initial sintering of the metallic powdered particles. As the metal particles are subjected to continued sintering process, densification and structural integrity of the porous structure is enhanced. The space holder properties like shape, size, and quantity can be varied to

improve the features of the foam. The setback associated with this technique is the difficulty in removing significant amount of space holder materials from the condensed mix [5].

1.5.2.5 Vapor Deposition

This technique can achieve a porosity of 75-85%, with a high degree of continuous interconnecting pores used for the fabrication of Trabecular Metals. This application is a function of the polyurethane medical grade. The polyurethane foam is eventually segmented into different shapes, when it is subjected to reticulation and pyrolysis, resulting in a less dense reticulated vitreous carbon (RVC) structure. The chemical vapor deposition (CVD) process, converts the RVC pre-foams into Trabecular Metal®, by supplying pure tantalum throughout the RVC pre-foams. In CVD, reactants are activated in the gaseous phase, undergoing a chemical reaction, and then solid materials are being deposited on a heated substrate [5].

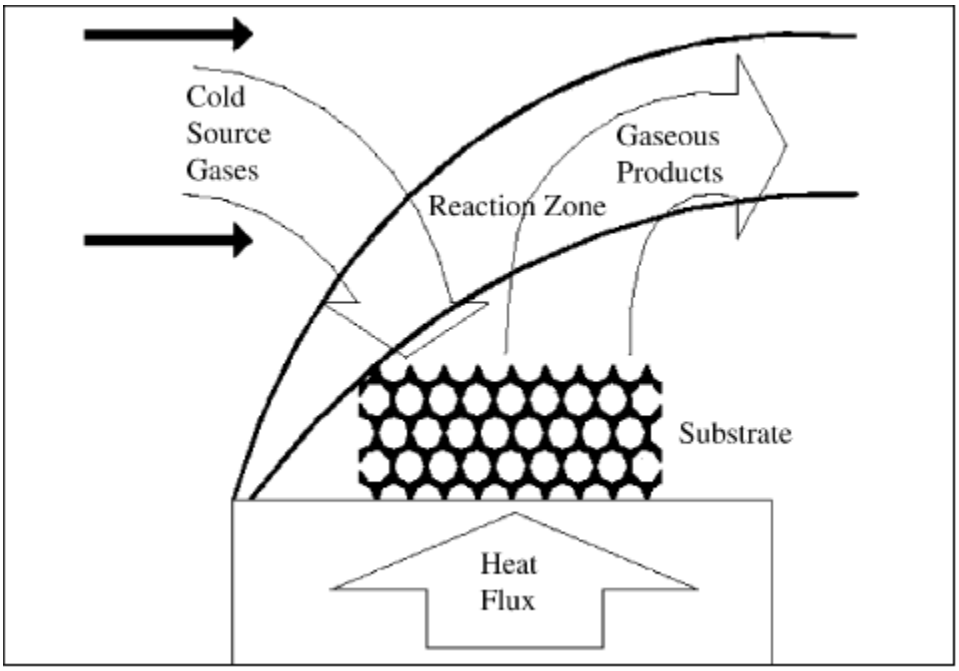

Figure 4. Schematic of the CVD process, utilizing intermediate reticulated vitreous carbon substrate. [5] Reprinted with permission.

1.6 Additive Manufacturing Techniques

Additive manufacturing, also termed 3D printing can be used to create end-use components, complex geometries from their CAD model, spanning across pore size, pore shape, interconnected pores, enhanced porosity, etc., making the mass production of customized porous implants possible. There are several rapid prototyping printing techniques available today, some of which are discussed below.

1.6.1 3D Printing (3DP)

This process involves a combination of powder materials deposited in layers and a binder material. Droplets of the water-based liquid binder are poured through an ink jet printing head onto the polymer or ceramic-based powders, at points where solidification is required, to produce parts from 3D CAD models [34, 35]. There are two types of inkjet printing systems explored by MIT; drop-on-demand and continuous-jet system.

1.6.2 Fused Deposition Modelling (FDM)

FDM is a 3D printing technique, in which a thin plastic filament is fed through the print head of the machine, and is melted by the print head, extruding it on a substrate, to form desired parts layer by layer. The thickness of each is usually 0.25mm. Materials utilized in this process are; PC-ABS blends, PC-ISO, ASA, ABS, polycarbonate, PPSF. This technique requires a post-finishing process for obtaining a smooth surface and is time demanding when producing large parts [2].

1.6.3 Selective Laser Sintering (SLS)

SLS technique, a powder-bed fusion process, sinters powdered particles to form a layer of part repetitively, using a focused CO_2 laser beam. To limit the amount of laser power input and deformation of the built part, build chambers are heated at an elevated temperature just before the

melting temperature of the material used for fabrication. A powder leveling scraper spreads the powder particles layer by layer across the powder bed [36]. The printing process which occurs at high temperature, takes place in a chamber filled with inert gas, nitrogen or argon gas, to prevent oxidation. A focused CO_2 laser beam scans the powdered material and then thermally fuses the material at positions based on the design specification. After each layer build, a piston lowers the completed layer build by the same amount of the layer thickness in the z-direction, allowing for the spread of the loose powder material for a new layer build. This process continues until the series of layers is completed and specified CAD design is produced. Varieties of materials such as plastic, metals, ceramics, and combination of this materials, have been utilized for direct metal laser sintering process. Unused powder materials can also be reused. Binders are used to hold metallic powder together during the SLS process and later removed. Many elements influence the accuracy of the part produced via this process, e.g., powder particle size [2].

1.6.4 Selective Laser Melting (SLM)

SLM, a powder bed fusion process [36], can produce close to fully dense structures, due to the laser beam fully melting the powders. SLM technique requires more substantial laser beam power input, thereby increasing energy cost. A moderate to excellent surface finish and feature resolution can be achieved via this technique. Also, polymers, metals, and ceramics can be utilized in this process for part production.

1.6.5 Electron Beam Melting (EBM)

The EBM processes are similar to the SLS process, as an electron beam melts the powdered particles, powered by a high voltage of 30 and 60 KV [2]. The printing process which occurs at high temperature and takes place in a vacuum chamber to prevent oxidation. The scan speed is

very fast, and the surface finish is moderate or poor [36]. This technique processes a high variety of pre-alloyed metals [2].

1.6.6 Laminated Object Manufacturing (LOM)

LOM technique combines traditional subtractive methods and additive manufacturing methods to fabricate or laminate layered parts. It processes models with papers, composites, and metals [2]. The material takes the form of a sheet of layers which can be bonded by thermal bonding, adhesive bonding, or ultrasonic welding [2]. The sheets represent the layered CAD models cross-section. CO_2 laser cuts the material matching the specified 3D CAD model and STL file per layer. This technique is relatively cheap and requires no post-processing, no support structures, nor phase change, but results to waste of material during the laser subtractive process, and the internal pores may be challenging to fabricate.

1.6.7 Laser Engineered Net Shaping (LENS)

LENS delivers powdered material into the focal point of ND: yttrium-aluminum-garnet laser to form a melt pool [38]. A metallic substrate serves as a base for the build [39]. The laser beam scans the substrate to form a weld bath of the base material, undergoing solidification upon cooling. Powdered metallic particles are then injected and absorbed into the molten pool [40], to build up each layer. Powder feeder supplies powder to the powder delivery nozzle assembly for a deposit on the substrate. When a layer of the geometry is formed on the substrate, the substrate moves in the z-direction below the laser beam, allowing, a new layer to be developed [39]. The build chamber is inert controlled, using argon gas with a reduced amount of oxygen, lower than 10 ppm. A wide range of metals such as Ti6AL4V, steel alloy, etc. can be used [2]. This process can also be used for part repair and to obtain functionally graded composite materials, feeding constituent materials from different powder feeders [41].

1.7 Biomaterials

Biomaterials form the basis of some medical devices, as they react with biosystems to help the body heal, in the form of tissue repair or the replacement of infected cells or organs [42]. Tissue scaffolds utilize materials consisting of metals, ceramics, polymers and their composites. If the requirements of biomaterials for tissue engineering applications are not met, this may lead to the failure of the implants, yielding to chronic pain for the patient and a revised surgery.

Biomaterial requirements can be grouped into mechanical and non-mechanical characteristics. It should possess a reasonable amount of fatigue strength, higher yield strength, and young modulus similar in value to the human bone [43]. Also, biomaterials should have a high resistance to corrosion as the body fluid is corrosive, making it a viable environment for the corrosion of implants [44].

Corrosion have an adverse effect on both the medical device and the human body, as the degradation of metallic ions can remain around the implants and be conveyed to other parts of the body [43]. The avoidance of implant loosening is dependent on factors, such as high wear resistance and a reduced coefficient of friction. As the wear particles react with and destroy the bone that provides support for the implant [45, 46].

Biocompatibility of implants with minimal adverse effects on the body cannot be overemphasized. Above all, it should support the formation of new bones and the recovery of bone from injury. A large surface area for biomaterials aids the integration of the surrounding bone to the implants in a well-fitted manner impeding the loosening of the scaffold [43].

1.7.1 Stainless Steel

Metals are electrically and thermally conductive with good mechanical properties. They also possess high specific gravity and high melting points owing to the strength of the attraction

of the metallic bond between the positive metal ions and free electrons [47]. Cold working can increase the hardness of 316l stainless steel, whose carbon content is 0.03% with improved corrosion resistance to chloride solution. Molybdenum contained in stainless steel allows resistance to pitting corrosion in salt water. 316l stainless steel material tends to corrode when subjected to highly stressed and oxygen-depleted regions in the body [47]. A significant application of stainless steel material can be seen in its use in temporary implants, an example is the fabrication of fracture plates, which hold together broken pieces of bone [47].

1.7.2 CoCr Alloys

CoNiCrMo and CoCrMo in the wrought and castable, are the two most common alloys used in implant fabrication. The latter has a comprehensive application in the manufacturing of dental implants and artificial joint. CoNiCrMo is a suitable material to produce prostheses, for load bearing applications. The solid solution of CoCr alloys is made up of 65% Co, the molybdenum is responsible for higher strengths, and its chromium content enhances its resistance to corrosion and solid solution strengthening. Hot forging is the only process that fabricates large implants using CoCr alloys, for example, hip joint stems. The wrought CoNiCrMo possess a high fatigue resistance, and a high ultimate tensile strength with durability, in the absence of fracture or stress fatigue. The release of metallic product from wear and corrosion may harm the human body, organ, or tissue, impeding cell functionality. In addition, the ductility of the alloy is reduced as the strength increases. The composition of Co and Ni at 50% concentration is more harmful than the Cr extract. The transfer of load to the bone possess a great concern [47].

1.7.3 Pure Ti and Ti6AL4V

Titanium is light and possesses good mechanochemical properties, making it suitable for implant production. Ti6Al4V alloy is made up of aluminum (5.5~6.5%) and vanadium (3.5~4.5%),

possessing the same fatigue strength as CoCr. The presence of impurities in Ti alloys increases strength and reduces ductility. Titanium alloys specific strength is higher than that of other implant materials, with titanium having a poor shear strength, not suitable for plates, bone screws, pins, etc. When in sliding contact with metals or itself, it galls and seizes. Micromotion may cause the release of TiO_2 particles in the bonded prosthesis, with the particles forming a periprosthetic fluid and enhancing cell response around the implant [47].

1.7.4 Ceramics

Ceramic scaffolds are applied in the dental field to fill defects in the bone and also in the orthopedic field to coat implants for improved fixation of the implant to the bone host [42]. They have a high mechanical stiffness, hard, brittle surface, and low elasticity. The chemical and structural composition of ceramics is like the mineral phase of the native bone, making it biocompatible with the bone. Ceramics enhances bone regeneration when in contact with osteogenic cells [48]. Ceramics in applications are limited by their brittleness, the difficulty of producing implants of complex shapes and the degradation rate cannot be controlled easily [42].

1.7.5 Synthetic Polymers

Synthetic polymers are PLGA, PLLA, polystyrene, and PGA [42]. Although its degradation features can be controlled, it has a low level of bioactivity resulting in rejection by the body. Through hydrolysis, carbon dioxide is produced by the breakdown of PGA and PLLA, and reduces the local ph., and may lead to the damage of human cells and tissue. Polymers cannot be subjected to high load bearing applications.

CHAPTER II

MOTIVATION AND OBJECTIVES

As discussed in the previous chapter, the discrepancy between Young's modulus of the host bone and solid metals is a drawback for metallic implants in the orthopedic field, yielding to failure in the performance of the implant, chronic pain for the patient and a revised surgery. Porous metals have been investigated, to reduce the elastic modulus, similar to that of the human body [5]. 3D printing serves as a potential alternative technique in overcoming the limitations of traditional manufacturing methods in producing and regulating complex internal structures that mimics the human anatomy.

The use of 3D printing in producing porous metallic parts is growing at a fast pace. This research focuses on porous metals for orthopedic application requiring load-bearing capacity, because of their superior fracture and fatigue resistance, and use in ultra-lightweight-strength metallic structures [28]. Porous ceramics cannot be utilized for loadbearing applications, due to their brittleness, and are not sufficient to meet the mechanical requirements of the human bone, although their chemical composition matches that of the mineral phase of the human bone. Polymer chains are also not capable of holding mechanical forces [5] and possess a low level of bioactivity. The objectives of this research are:

- To investigates the effect of 3d printing on the pore architecture of varying sizes.
- To investigate the cell growth viability of the 3D printed 316L stainless steel porous materials using SLM technique.
- The effect of pore sizes on the biological performance of Pseudomonas aeruginosa cells seeded on selective laser-melted 316L stainless steel scaffold models.

This research utilizes the SLM technique to fabricate porous structures, which were then exposed to cell culture experiment to facilitate seeding of the samples with Pseudomonas aeruginosa cells to test for cell adhesion and cell enumeration in CFU. This study will guide future research to control the process parameters and design, to attain optimal pore architecture for cell growth viability and support. The specific technical approaches are as follows:

1) Design and analyze the surface morphology/melt pool of the 316L stainless steel porous structure.
2) Measure the actual 3D printed 316L stainless steel pore sizes in comparison with their initial CAD file dimensions.
3) Evaluate the cell growth of 316L printed porous structures and optimum pore size for cell growth.
4) Analyze the corrosion rates of 316L corrosion rate and their effect on cell viability
5) Evaluate underlying factors for biological responses of the 3D printed structures.

The experimental methods will be expanded in Chapter III.

CHAPTER III

EXPERIMENTAL PROCEDURES

This chapter reveals the material and experimental methods utilized in this study. Stainless steel powdered materials with a mean diameter of 35µm were used to fabricate the porous structures, via the selective laser melting technique. The experimental approach includes the design of the porous structures, actual 3D printing process, SEM characterization, corrosion test, etc. Figure 5 shows a flowchart summarizing the activities involved in this research. Experimental details and procedures are explicitly detailed.

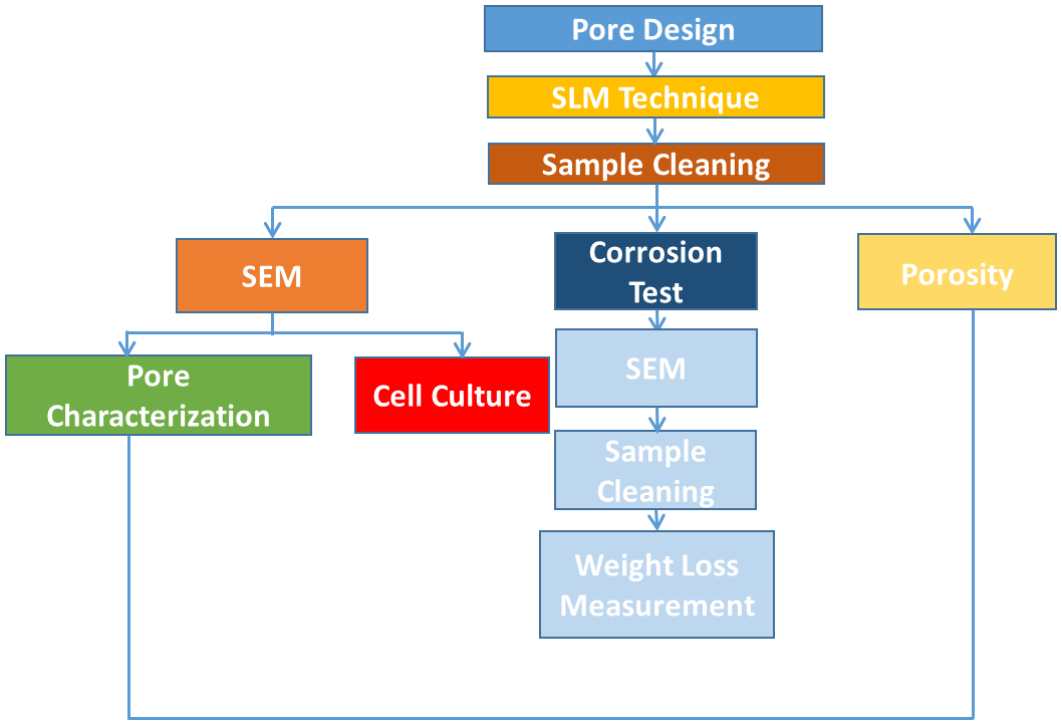

Figure 5. Experimental flow chart illustrating the process of designing, manufacturing and testing the porous 316L stainless steel structures utilized in this study.

3.1 Materials

The 316L stainless steel powder distributed by Renishaw, plc. was used in this research. The readily availability of 316L stainless steel, alongside with its other advantages which will be discussed further in this text, makes it a suitable material for use in the medical field. Naturally, occurring steel, possess great tendency to corrode, to increase its corrosion resistance properties, alloying metallic elements such as iron-chromium, nickel, carbon, etc., are added to produce stainless steel [49]. On the surface of stainless steel material, it forms a passive film of chromium oxide layer, upon exposure oxygen, to enhance self-repair, making the steel corrosion resistant.

Stainless steel materials are subdivided into various groups, dependent on the composition percentage and microstructure of the alloys added, such as carbon, nickel, chromium, molybdenum, etc. Since chromium is responsible for enhancing the corrosion resistance of steel, by creating a passive film of chromium oxide, a minimum of 10.5% of chromium is required. Nickel improves ductility, toughness, strength and corrosion resistance of steel at elevated temperature. Examples of corrosion-resistant stainless-steel samples are; Type 304, Type 430, Type 316, and Type 630. As stated earlier, this research utilized 316L stainless steel powdered material. At elevated temperature, Type 316 and 316L, an austenitic steel alloy, possesses high creep and tensile strength, good weldability and formidability. 316 stainless steel varies from 316l stainless steel in its carbon content of 0.08% & 0.03% respectively with the latter having a higher resistance to corrosion. 316L stainless steel has a nickel composition of 10-14% and molybdenum content of 2-3% (see Table 1) than other types of stainless steel in its grade. Its composition provides room for higher corrosion resistance than Type 304 with respect to pitting and crevice corrosion [49]. 316L stainless steel powder can be applied in AM techniques to create customized implants and prosthesis for patients at low cost [50]. The 316 stainless steel material relative

density of 99.90 and 99.95% has been achieved via the SLM technique. SLM stainless steel parts possess higher strength and are less malleable than their forged counterparts. SLM process of 316L stainless steel undergoes rapid cooling and solidification, leading to a more refined cellular dendritic microstructure, and ultimately improving the tensile strength of the fabricated part [50]. The surface roughness of the material reduces as the laser power of the SLM techniques increases. Table 1 shows the makeup of 316L stainless steel utilized in this research

Table 1. 316l Stainless steel composition. Redrawn from [52]

Element	Mass Composition (%)
Iron	Balance
Chromium	16.00 - 18.00
Nickel	10.00 - 14.00
Molybdenum	2.00 - 3.00
Manganese	<2.00
Silicon	<1.00
Nitrogen	<0.10
Oxygen	<0.10
Phosphorus	<0.045
Carbon	<0.03
Sulphur	<0.03

3.2 Design of Porous Structures

Four cubic models (scaffolds) of 15×15×4 mm^3 were designed, with interconnected pore sizes of 0.4 mm, 0.6 mm, 0.8 mm and 1.0 mm, respectively (see Figure 6 and Table 2) using Inventor CAD Design software. The CAD model produced is saved as an STL file. In the case of porous materials, the size of the STL file becomes huge due to a large number of features. Choosing an STL resolution is, therefore, a function of file size and geometric accuracy. The size of the CAD file and geometric accuracy are important factors to consider in the selection of STL

resolution. QuantAM software processes the STL models to produce build-files for the SLM machine.

Table 2. Design parameters.

Pore size (mm)	Length (mm)	Width (mm)	Thickness (mm)	No. of pores in length	No. of pores in width	No. of pores in thickness	Pore spacing (mm)
0.4	15	15	4	32	32	6	0.46
0.6	15	15	4	21	21	4	0.69
0.8	15	15	4	15	15	3	0.92
1	15	15	4	13	13	2	1.15

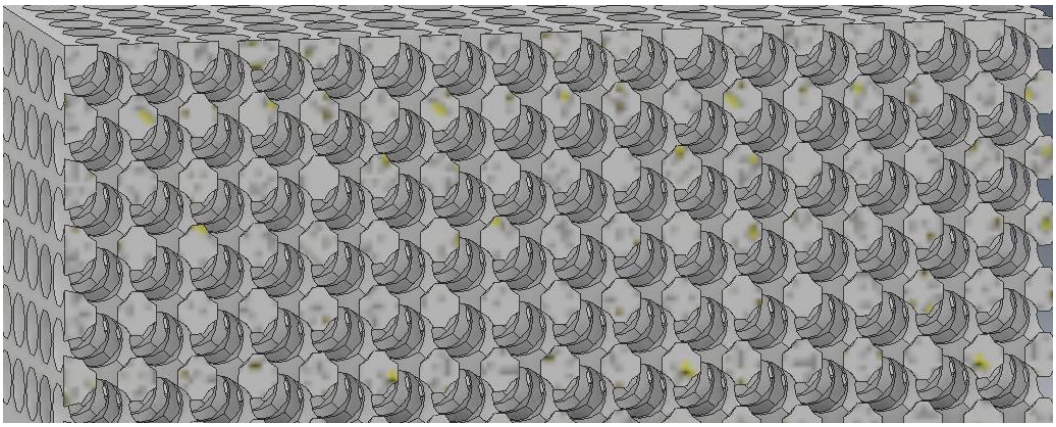

Figure 6. Quarter section view of 0.4 mm pore size CAD model.

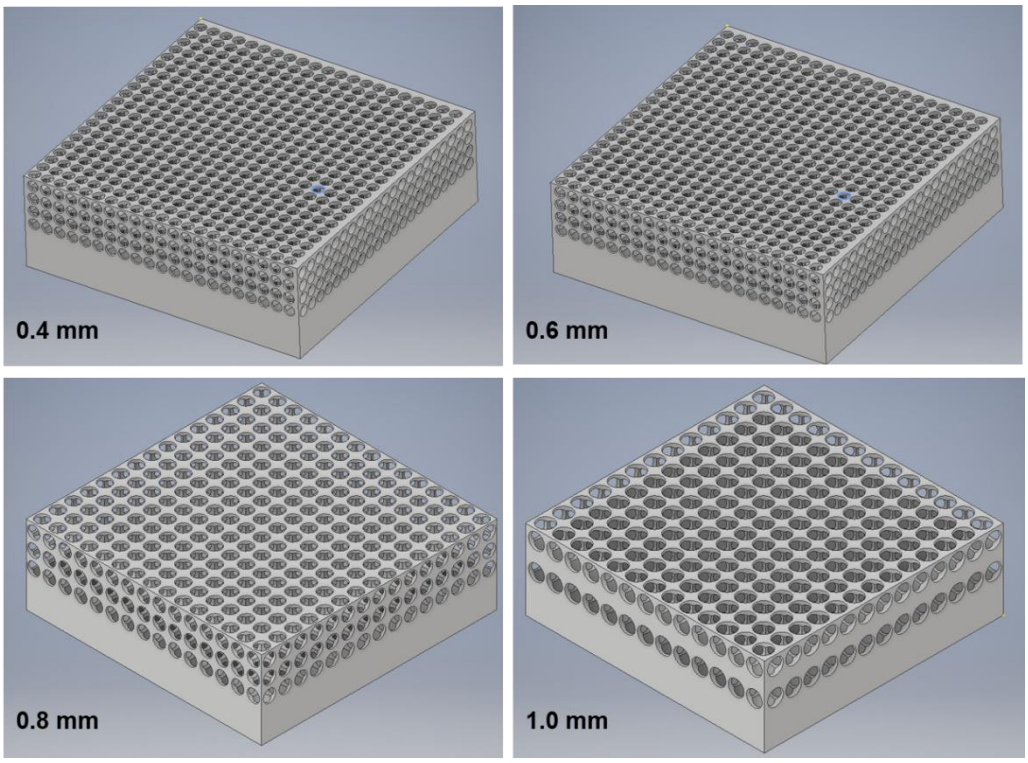

Figure 7. Cubic scaffold models designed for this study.

3.3 Selective Laser Melting Technique

The porous structures were fabricated at the same time, using Renishaw AM400 selective laser melting (SLM) machine (see Figure 8), with the imported and converted STL CAD models. Renishaw QuantAM software prepares printing instructions for the SLM machine by slicing the model into layers of 50µm, depending on the height of the designed model. Then it produces scan paths that serve as a guide for the scanning process of the laser beam on the 316l stainless steel powdered material. The developed scan instructions (path, power levels, exposure times, and so on) are compiled into a build file for the machine. SLM techniques require no post-build sintering

to achieve near cast density, as the powdered metal is intended to melt completely by the laser beam.

The build envelope of the 3D printer used in this study is 250×250×300 mm^3 (W×D×H) and utilizes a pulsed laser. Argon gas fills the build chamber, during the printing process to avoid oxidation and the only source of heat in the chamber is produced from the laser beam. Layers of metal powder are distributed and leveled on the powder bed using a powder scraper. Excess powder that drops from the powder bed is collected into a flask for recycle. The laser beam melts the powder, which in turn re-solidifies to form the porous structures, during the laser scanning process.

A mild steel substrate holds the layered parts formed. After each layer build, a piston lowers the powder bed in the z-direction by 50 µm layer thickness, allowing for the fresh deposition of the 316L stainless steel powdered material on the previously created build layer, for a new layer build. This process continues until all features of the required CAD design is produced and required geometry generated (all series of layers completed). Powder that hasn't been scanned, but serves as a support structure for the new build, and surrounds the completed geometry, is swept away when the piston rises for the fabricated porous structures to be removed. Further excess loose powders were removed using a brush and a vacuum cleaner which is collected in a powder flask available in the machine for reuse.

Figure 8 shows a representation of the SLM machine used to fabricate the porous structures.

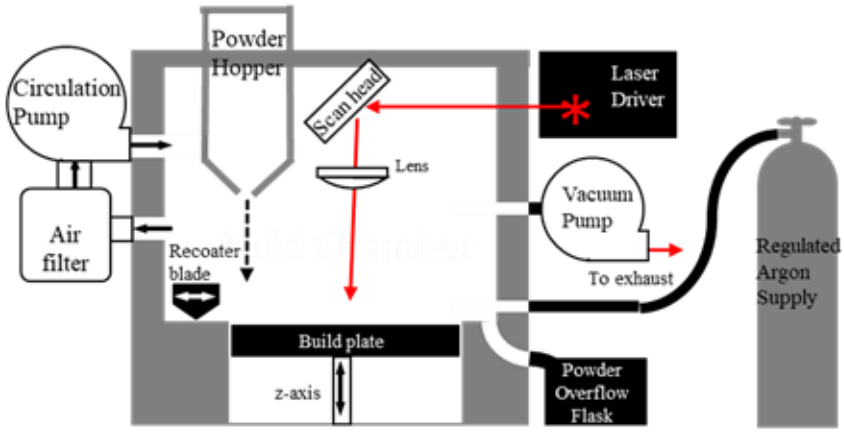

Figure 8. Selective laser melting machine schematic diagram.

Every step can affect the quality of the manufactured parts as material characteristics, and processing parameters influence the properties of the printed structures[53]. These are dependent on the processing parameters of the printing process. Table 3 shows the build process parameters specific to this study, to produce the porous structures. Different scan paths may vary in their process parameters, which can be further divided to generate other parameters. For example, the average scan speed of the border is lower than that of the fill. The pulsed laser applies energy in discrete locations, but the result is like that of a continuous laser. It is useful to provide an average laser velocity to compare the energy density with other laser melting processes. The average scan velocity is calculated using Equation 1.

$$v_a = \frac{d_p}{t_e + \left(\frac{d_p}{v_j}\right)} \quad (1)$$

where v_a is the average scan velocity, d_p is the point distance, t_e is the exposure time, and v_j is the jump speed.

Table 3. SLM processing parameters. Redrawn from [52]

Printing Parameters	Parameters
Laser Beam diameter (µm)	70
Laser Beam Power (W)	200
Hatch distance (µm)	110
Powder layer thickness (µm)	50
Powder particle mean diameter (µm)	35
Average Scan Velocity (µm/s)	0.75

3.4 SEM Characterization

The morphology of the surface, actual sizes of the pores and melt pool, were characterized with a scanning electron microscope (SEM) at various magnification. The exact pore sizes s on the structure surface from the SEM images, were analyzed using Image J. ATESCON VEGA II LSU SEM with a magnification of 13 x 10^0 to 1 x 10^6 and a scanning velocity of 160 ns to 10ms [54].

3.5 Salt Spray Test

The accelerated corrosion test technique used in this study is a quick way to determine the rate at which the porous structures will corrode. The salt spray chamber comprises a fog chamber, atomizers, salt solution reservoir, a supply of compressed air, and chamber temperature regulator. A 5 wt. % salt (NaCl) concentration (Ph between 6.5 and 7.2) for 5000ml of purified water (see Equation 2) provides a corrosive environment for the metallic porous structures and is atomized by spray nozzles via pressurized air in the form of brine fog. 789.48g of pool salt was mixed with

15 liters of purified water to top up the brine solution inlet, while the bubble tower inlet was topped up with purified water almost to the brim.

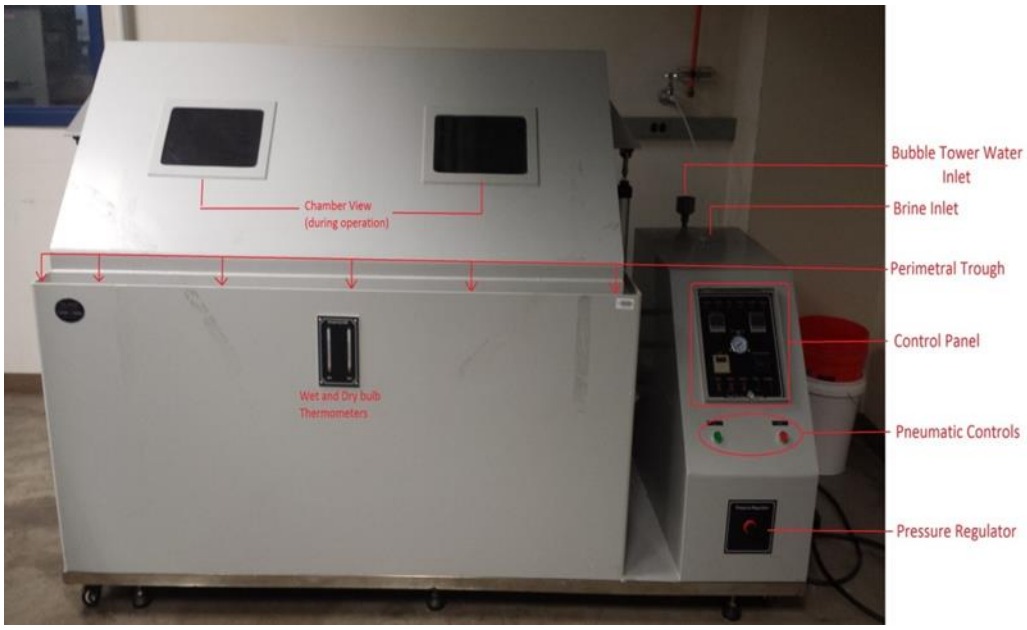

Figure 9. Salt spray equipment exterior view.

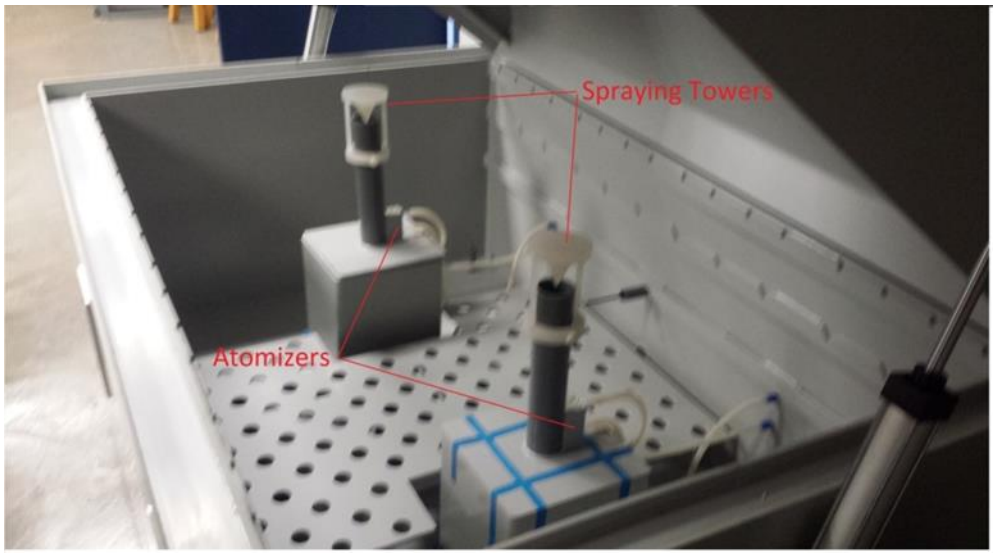

Figure 10. Salt spray equipment interior view.

The samples placed in the salt spray chamber for exposure to the corrosive environment conditions were removed after 14 days (336 hours), to evaluate the corrosion rate. The chamber temperature operated at 35^{o}C, while the bubble tower temperature operated at 30^{o}C. For every three-day interval, the salt-water inlet is topped up, as well as the bubble tower inlet.

$$X_g = \frac{wt\% * v_p}{100 - wt\%} \quad (2)$$

where X_g is the mass of salt (g) and v_p is the volume of purified water (ml).

The corrosion rate of the samples was determined using the equation below [55]:

$$Corrosion\ rate\ (mpy) = \frac{W}{A*t*\rho} * 534 \quad (3)$$

Where w is the weight loss (mg), ρ is the density of 316L stainless steel (7.99g/cm^3), A is the area (in^2), t is the exposure time (336 hours), 534 is the conversion factor, to derive units of corrosion rate in mils penetration per year (mpy) or milli inch per year. The rate of penetration or thinning of the metal part reveals the service life of a component.

3.6 Porosity

The porosity measurement of each sample was determined experimentally from the relative density of the printed structures and that of the specified 316l stainless steel material presented in Equation 4. The samples were redesigned with SolidWorks according to the actual size parameters obtained from the SEM image analysis of the 3d printed parts. An alternative theoretical method for porosity calculation, as shown in equation 6, is the pore volume fraction [56]. The Evaluate

tool of SolidWorks gives the physical properties of the models like theoretical volume, density, mass, and surface area of the 3D models.

The mass utilized in deriving the experimental porosity via the relative density method was obtained using a weight measurement scale with a high accuracy of 0.1 mg. It is advisable to use the experimentally derived porosity values as this value has a higher dimension of accuracy values, taking into consideration the processing conditions and effects of the laser melting technique. Another technique used to compute the relative density and structures' porosity is the Archimedes method, as this method enables the density of complex structures to be derived, without having to determine their volume, which may be difficult to derive, due to complex geometries. Firstly, the mass of a sample is measured in the air, which is called the dry mass (m_d). The sample is then suspended in water to determine its wet mass (m_w), which is the dry mass minus the buoyancy from water (see Equation 7).

$$\boldsymbol{Porosity} = \left(\mathbf{1} - \frac{\boldsymbol{\rho_s}}{\boldsymbol{\rho_m}}\right) * \mathbf{100}\% \tag{4}$$

$$\boldsymbol{\rho_s} = \frac{\boldsymbol{m_s}}{\boldsymbol{v_t}} \tag{5}$$

$$\boldsymbol{Porosity} = \frac{\boldsymbol{v_p}}{\boldsymbol{v_t}} * \mathbf{100}\% \tag{6}$$

$$\boldsymbol{\rho_s} = \boldsymbol{\rho_{wt.}} \frac{\boldsymbol{m_{ds}}}{\boldsymbol{m_{ds}} - \boldsymbol{m_{ws}}} \tag{7}$$

$$\boldsymbol{v_t} = \boldsymbol{v_s} + \boldsymbol{v_p} \tag{8}$$

where ρ_s is the scaffold's density, ρ_m is the 316L stainless steel material density (7.99g/cm^3), ρ_{wt} is the density of water, m_s is the mass of the scaffold, m_{ds}& m_{ws} is the dry mass and wet mass of the scaffold. v_t is the scaffold's total volume, v_p is the pore volume, v_s is the scaffold's volume.

3.7 Cell Culture

To study SLM technique and pore architecture effects, on cell adhesion, the porous samples were wrapped in aluminum foil and dry autoclaved to achieve sterilization. Duplicates of each sample were provided, and one set was used for colony forming units (CFU) enumeration while the second set was processed for SEM analysis.

Pseudomonas aeruginosa strain PAO1 was inoculated from glycerol stocks onto Luria LB agar plates and incubated at 37 °C overnight. Bacterial inoculum was obtained by picking a single colony from the initial inoculum formed and used to inoculate the liquid LB media overnight at 37 °C.

The sterilized samples were placed in a segmented well, and 5ml of overnight bacterial culture, diluted to an optical density of 0.01 in LB was dispensed into the wells. The plate was covered and incubated at a temperature of 37 °C for 48 hours to facilitate enhanced biofilm formation. The discs were then retrieved using sterile forceps and subjected to three PBS washes to remove loosely attached bacteria. After post-wash, the samples were inserted into a 50 ml cylindrical tube with 5 ml PBS and vortexed thoroughly to dislodge the bacterial biofilm. For the first set of the sample, the bacterial suspension thus obtained was diluted appropriately and 50 µl of the dilution spotted on to the LB agar in triplicates for bacterial enumeration and quantification.

While the second set of the porous samples were washed as detailed above and then dipped in 2 % v/v of glutaraldehyde to enable bacterial fixation. SEM techniques was used to examine the cells grown on the samples.

CHAPTER IV

CHARACTERIZATION OF 3D PRINTED POROUS 316L STAINLESS STEEL

4.1 Melt Pool

The melt pool of the 316L stainless steel material is shown in Figure 11. The surrounding powdered material deposited on the substrate was melted by the laser beam to create a melt pool, which then cools rapidly and solidifies to form the pores. In this process, a greater amount of radiation is transformed into thermal energy to create the molten pool. A laser power of 200 W was utilized for this study, the melt pool diameter along a single bead is non-uniform and irregular (instability of scan tracks), with an increased magnitude at the beginning and end points of the molten region. The start and end points of the melt pool are wider, while the melt pool is rounded at just the start point. The fluctuation in the scanning speed or exposure time, i.e., the amount of time for which the scanned point is exposed to the laser beam, gives rise to the rounded start points and wider endpoints, during the transition from one bead to another [57]. The term, exposure time will be used in this research, rather than scan velocity, as a pulsed laser is associated with the 3D printer used to fabricate the porous structures. The different melt pools on each sample are uniform and consistent.

The melt pool geometry was observed and measured using SEM and Image J respectively and quantified to be approximately 250 μm in width (diameter), in contrast to the melt pool diameter specified by Renishaw for the AM400 metallic 3D printer for its printing processes. For Ti-64 material, the combination of lower scan speeds and higher amount of laser power leads to wider melt pools and another combination of higher scan speeds and lower laser power may lead to a reduced or narrow melt pool [57].

As stated earlier, for this research, a pulsed laser was used, and the average scan velocity can be obtained via the ratio of the distance between points exposed to laser power, to the sum of the exposure time and the ratio of the point distance to the jump speed. The exposure time for a 200W laser power, utilized in this study is 80 ms, the point distance is 60 µm, the jump speed is 5 mm/s. This is a combination of low exposure time and higher laser power leading to a wider melt pool, with the laser power having a greater effect as shown in Figure 11. The diameter of the molten pool increases due to the high laser power density and thermal diffusion from the points of powdered material being scanned by the laser beam, to the surrounding metallic powdered particles. The properties of SLM produced part, such as melt pool characteristics is a function of the energy density, controlled by the processing parameters such as laser beam diameter, exposure time, point distance, scanning pattern, hatch distance, powder shape, powder size, powder layer thickness, powder bed temperature, etc. Linear laser energy density (LED) and Areal energy density (AED) is the energy applied to the powder material per length and per area respectively during laser scanning, which defines the quality of built parts. The LED depends on the laser power, point distance and exposure time, for a single line scan, and is referred to as the linear laser energy density (LED) (see Equation 9).

$$\boldsymbol{LED = \frac{P.t}{d_p} \qquad J/mm} \tag{9}$$

$$\boldsymbol{AED = \frac{P.t}{d_p . d_h} \qquad J/mm^2} \tag{10}$$

Where P is the laser power, d_p is the point distance (distance between two points exposed to the laser beam), t is exposure time, d_h is the hatch distance (the distance between the centers of two adjacent scanning tracks and is expressed in units of length or percent overlap).An increase in power results to a faster melting rate and depth of heat penetration.

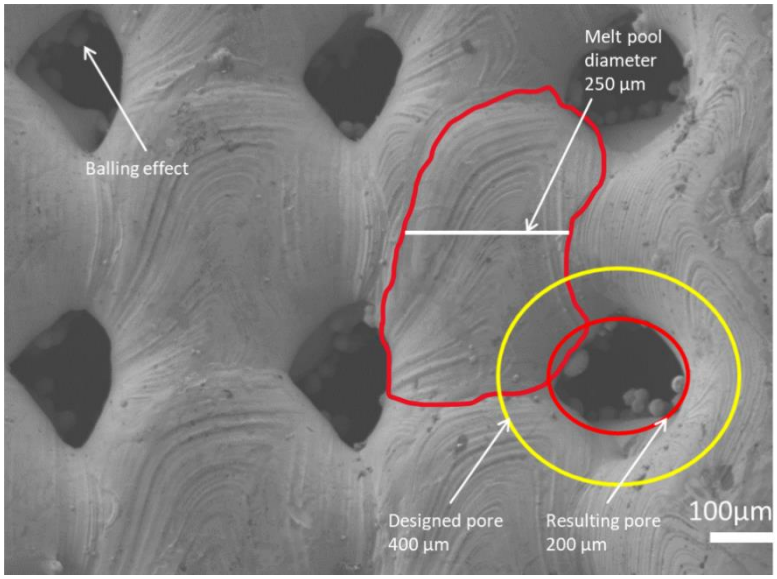

Figure 11. SEM characterization of 316L stainless steel 3D printed parts.

4.2 Balling Effect

Spherical balls can be seen in and around the pores of the 3D printed structures as shown in Figure 11. This occurrence is referred to as the balling effect, which has a negative impact on the texture of the material. Balling effect increases the roughness of the part, decreasing the mechanical properties and lifespan of the porous structures [58]. The melt pool temperature is dependent on the type of laser and its interaction with the powder. In this research, a significantly

higher laser power of 200 W creates a continuous wider melt pool, because of the exposure time and power of the laser spot on the irradiating region.

A phenomenon responsible for balling effect is incomplete melting caused by thermal diffusion. Due to thermal diffusivity of the metallic powder, there is a reduced amount of heat penetration depth and low-temperature gradient at powder locations far from the scanned region resulting to partial melting or moderately melted agglomerates. Also the non-uniform temperature distribution, due to heat transfer between the surrounding loose powders and the laser scanned parts, enhances thermal diffusion, responsible for the incomplete melting of the metallic powder at the surrounding region far from the scanned point [59], leading to balls of loose powders attached to the surface. The lower layers have rougher surfaces due to the tendency of the SLM material to experience either complete or partial melting, depending on factors such as the distance between points exposed to the laser beam, scan speed, exposure time, laser power, energy density, melting temperature of the material, laser beam diameter, etc.

Balling effect can be controlled based on the nature of the balling. One of the suggested ways to eliminate balling will be to increase the exposure time, as an increase in laser power and exposure time can increase the energy input, resulting in a complete melting of the 316L stainless steel material, due to a high scanning temperature above the solidus region of the material. In this case, the molten pool is fully liquid, which is easy to flow, spread and wet the surrounding un-melted metallic particles, yielding a fully bonded scanned part, free of any balling effect.

Another technique for eliminating the balling effect, is by decreasing the applied powder layer thickness for multi-layer parts. For multi-layer part and pulsed layer, a new term used to explain the influence of laser power (P), exposure time (t), hatch distance (d_h), point distance (d_p) , layer thickness (th), is referred to as volumetric energy density (VED, ε), given below [59]:

$$\varepsilon = \frac{P.t}{d_h.d_p.th} \quad (11)$$

A tentative reasoning reveals that powder layer thickness reduction can enhance the laser energy intensity per melt volume, ensuring a thinner layer of metallic powder to be fully melted and a dense fused structure to be achieved, void of balling effect, due to the sufficient optical penetration of the laser beam. The layer thickness for the SLM technique utilized in this study is 50 μm, yielding a low VED, creating a steep temperature gradient of low operating temperature at the underlying surface of the bottom layer and high heat on the top surface. Some of the bottom layer powders may be partially melted and not completely bonded together but stick to the surrounding pool upon solidification because of the low-temperature gradient at that depth.

4.3 Pore Size Characterization

The scaffolds, designed for outer dimensions of 15×15×4 mm^3, did not reduce in size as revealed in Table 4. The observed reduction in thickness is owed to the fact that the printed parts were removed from the substrate, via the wire EDM cutting technique.

Table 4. 3D printed scaffold external dimensions.

Pore size (mm)	0.4	0.6	0.8	1.0
Length (mm)	15.20	15.24	15.25	15.27
Width (mm)	15.22	15.21	15.27	15.23
Thickness (mm)	3.84	3.68	3.84	3.89

Figure 12 and Figure 13 shows the resulting SEM and white light interferometry images of the interconnected porous 316L stainless steel parts produced via the SLM process. A quantitative

image analysis using Image J was carried out to determine the AS printed pore size using a spectrum of SEM measurements (70 assessments for the designed pore of 0.4 mm, 60 for 0.6 mm, 80 for 0.8 mm, 46 for 1.0 mm) using Image J. Figure 12 and Table 5 show the measured pore sizes from the SEM images, compared with their CAD models. The analysis shows that the actual mean pore size reduced by 0.220 mm for all samples, compared to their 3D designed pore sizes (see Figure 14). The percentage pore size reduction is as follows; a 55% reduction for the pore size of 0.4 mm, 36% for 0.6 mm, 29% for 0.8 mm, and the largest pore possesses a 22% pore size reduction. As the pore size decreases, the percentage size reduction increases.

The 1.0 mm porous sample shows more rounded holes and a more uniform pore distribution than the smaller pore sizes (see Figure 12). The farther the distance of the melt pool from the pore or the larger the pore spacing, the more uniform the pores will be, because a greater amount of the surrounding metallic powder is not affected by the heat from the laser for the larger pore sizes, thereby preventing a larger percentage of pore size reduction. As the scan line distance increases, the interconnectivity, and uniformity of the pores increase, in the case of this research, more regular holes, and uniform pore distributions are obtained for larger pores sizes, as it increases from 0.4 mm to 1.0 mm,

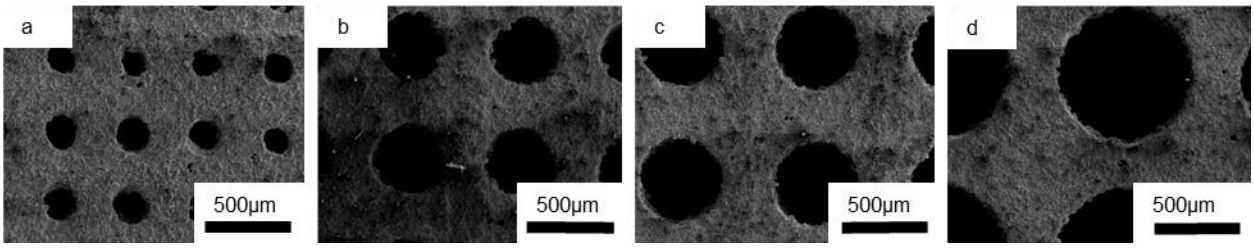

Figure 12. SEM images of 3D printed porous samples with various designed pore sizes: (a) 0.4 mm (b) 0.6 mm (c) 0.8 mm and (d) 1.0 mm.

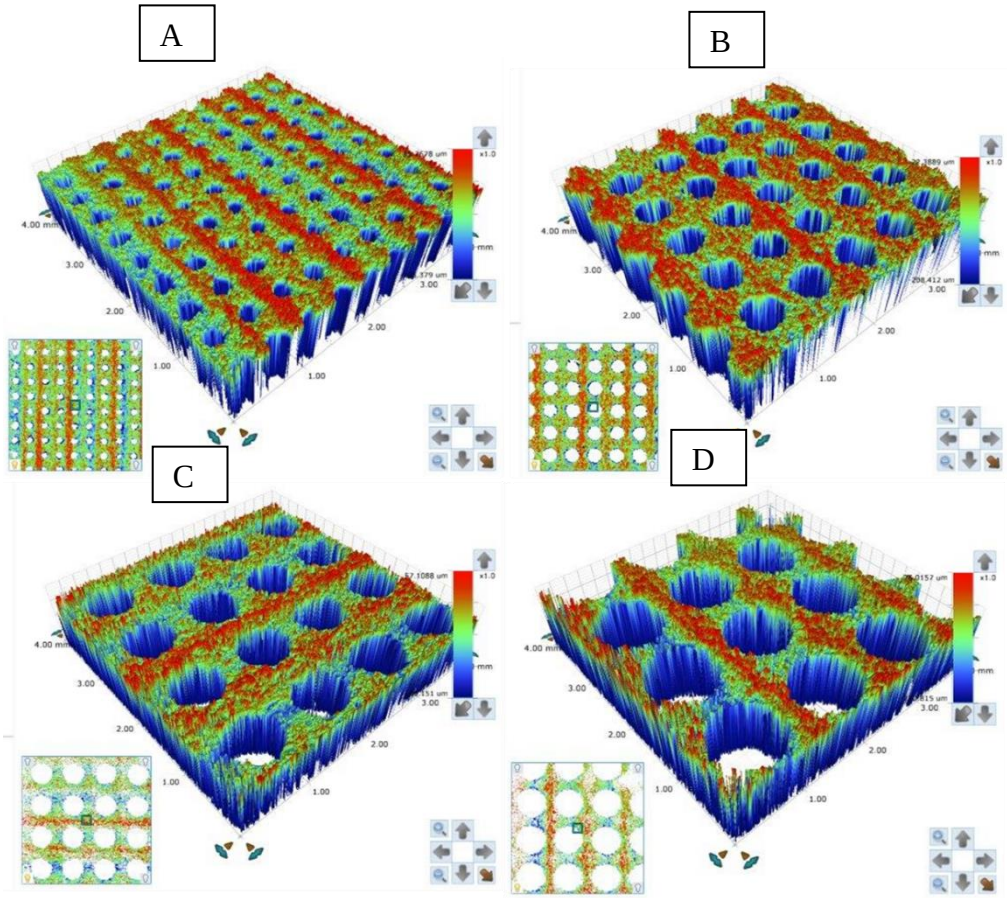

Figure 13. White interferometry of the 3D printed 316L porous structures (a) 0.4 mm (b) 0.6 mm (c) 0.8 mm (d) 1.0 mm.

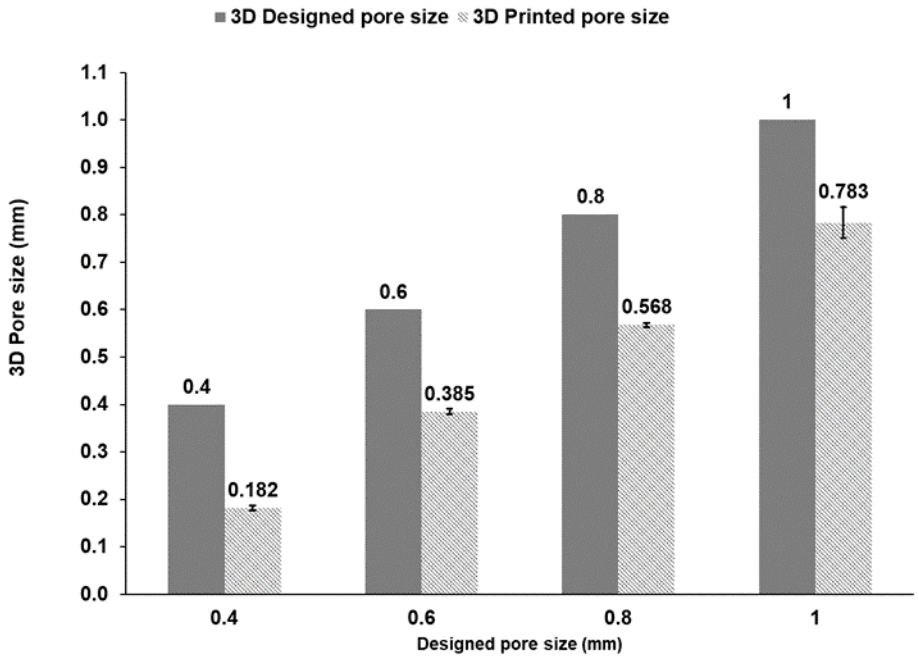

Figure 14. Graph showing the relationship between 3D designed and printed pore size.

Table 5. Summary of the 3D printed mean pore size.

Designed pore size (mm)	Printed pore size (mm)	Size difference (mm)	Size reduction (%)
0.4	0.182±0.024	0.218	54.6
0.6	0.385±0.023	0.215	35.8
0.8	0.568±0.021	0.232	29.1
1.0	0.783±0.109	0.217	21.7

Thermal diffusion is a phenomenon that occurs because of the heating of surrounding metallic powder, due to the heat transfer from the laser scanned surface to the surrounding material, enlarging the melt pool and increasing the thickness of the solidified part, which in return reduces the pores (see Figure 15). The melt pool diameter of the porous structures measured as 250 µm, which doesn't conform to Renishaw AM400 specified melt pool diameter of 50 µm, is responsible

for the pore size reduction of approximately 0.220 mm for each sample. As discussed earlier, the melt pool characteristics is a function of factors such as laser power, scan velocity or exposure time, hatching distance, powder layer thickness, thermal diffusion, etc., controlling the process parameters will aid the optimization of pore architecture, mechanical properties and functionality of the porous structures. Melt pool width and depth increase, with an increase in laser power and exposure time and decreases as the point distance, layer thickness, and hatch distance increase.

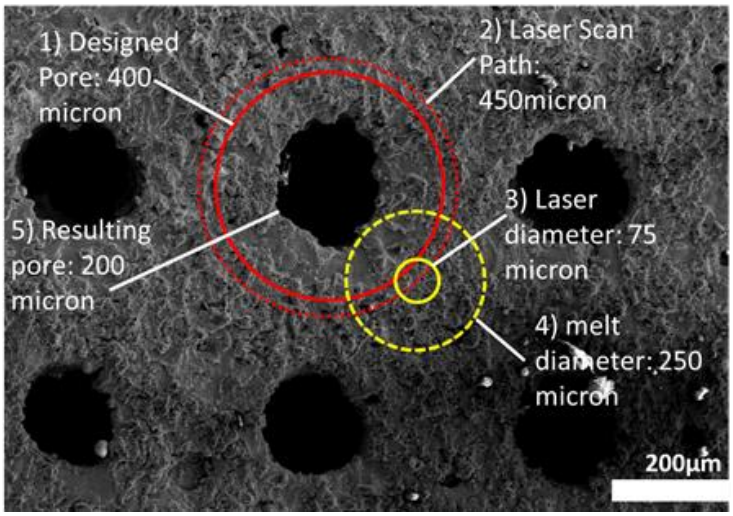

Figure 15. 3D Printed 316L stainless steel porous structure SEM image with an intended pore size of 0.4 mm and actual pore size of approximately 0.2 mm after printing.

Taking into consideration the printing error in pore size of 0.22 mm, if the same processing parameters will be reused as specified in this research, then the pore size must be greater than 0.22 mm, to be able to produce significant pores. As the pore size increases, the holes become well defined and uniform in shape.

CHAPTER V

BIOCOMPATIBILITY OF 3D PRINTED 316L STAINLESS STEEL POROUS STRUCTURES

The biocompatibility of the printed 316L stainless steel samples for cell adhesion and the effect of pore sizes on the biological performance of Pseudomonas aeruginosa cells seeded on selective laser melted 316L stainless steel scaffold models, are evaluated in this chapter. The influence of pore architecture fabricated by the SLM technique on porosity, corrosion rate and their impact on cell growth will be discussed. Cell culture experiment will be utilized to study and analyze the viable pore size for cell growth and support. Data obtained during the porosity calculation, salt spray accelerated corrosion test and cell culture experiment will also be presented in this chapter.

5.1 Effect of Pore Size on Porosity

Porosity is an essential requirement in implants, as they require highly interconnected porous environment in a well-organized structure, for cell support, cell growth, transfer of nutrients and waste. The designed pore sizes of 0.4 mm, 0.6 mm, 0.8 mm, and 1.0 mm were reduced to mean pore sizes of 0.182 mm, 0.385 mm, 0.568 mm, and 0.783 mm respectively after going through the SLM printing process. The porosity increases as the pore sizes increases with decrease in relative density as shown in Figure 16. Table 6 shows the calculated porosity values for the samples of varying pore size ranging from 34.3% – 61.2%. Porosity value for the 0.783 mm porous structure, possess a maximum amount of 61.2% due to its large pore size, whereas the smallest mean pore size value exhibits a much lower porosity of 34.3%. Its increased density limits the number of empty spaces or the percentage of the total volume that is made up of pores.

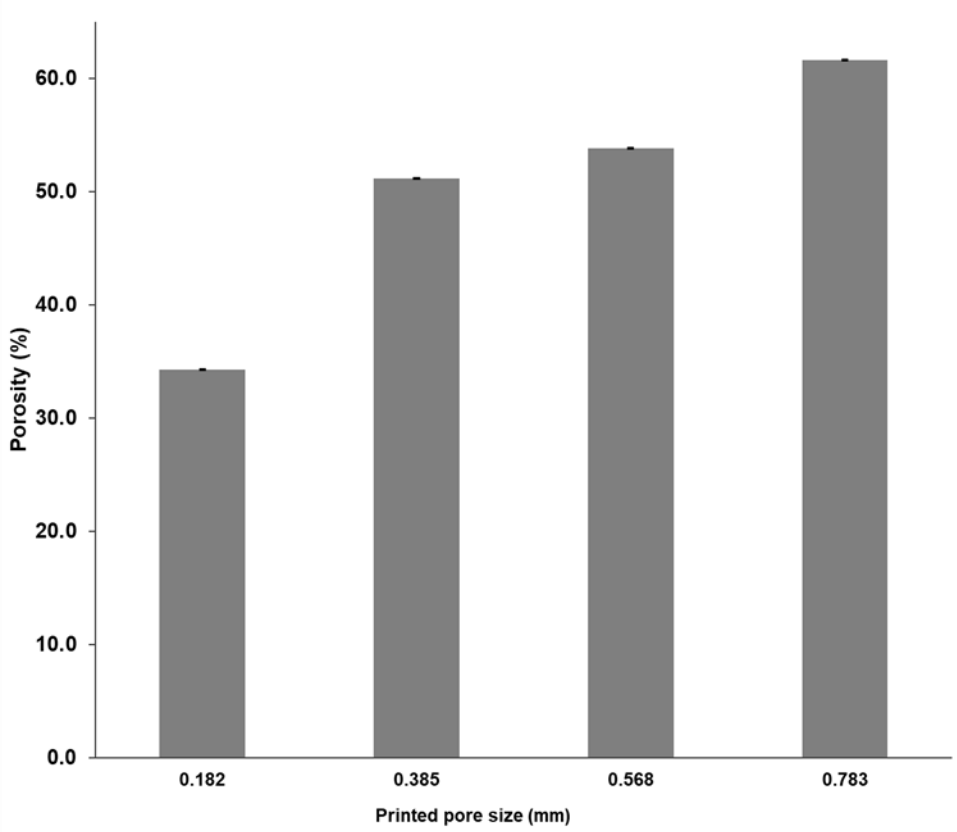

Figure 16. Dependence of porosity on pore size of 3D printed porous structures.

Porosity on the printed structures can occur due to factors such as structural design, controlling laser process parameters and the type of 3D printing technique used. A higher porosity or a decrease in density can be obtained by increasing point distance and hatch distance, decreasing the power of the laser and exposure time [60]. From the LED and VED equation analyzed in Chapter 4, a decrease in the exposure time, allows a limited time of laser power on the metallic powder, leading to less energy density on the powder, so the powders are not subjected to complete melting. These leads to the partial bonding of the metallic powder layers and increased porosity. The SLM technique produces samples of reduced porosity, due to the ability of the method, in producing fully dense parts of up to 99.95%. The porosity of the samples used in this study results

majorly from the varying pore sizes. Porosity can be controlled, to meet the requirements of biomedical devices, by designing interconnected pores of different width, or by controlling the processing parameter.

Table 6. Porosity trend parameters.

Pore size	Sample Mass (g)	Volume (mm^3)	Relative density	Porosity %
0.182	4.673	888.4	65.7	34.3
0.385	3.335	853.6	49.1	50.9
0.568	3.313	894.2	46.3	53.7
0.783	2.805	904.7	38.8	61.2

5.2 Effect of Pore Size on Corrosion Rate

Corrosion resistance is a major requirement for biomedical devices, as the release of metallic ions, from the degradation of metals is toxic to the human body and can result in the failure of the implants. The corrosion mechanism of each of the samples exposed to the accelerated corrosion test in a brine solution, reveals a uniform, erosion and pitting type of corrosion as the whole surface corroded with an insignificant weight loss (see Figure 17 and Figure 19). The results show an average corrosion rate of 3.00 mpy. The 0.182 mm mean pore size has the highest surface area of 4305.73 mm^2, with a corrosion rate of 2.92 mpy, 0.385 mm, 0.568 mm and 0.763 mm pore sizes with a surface area of 3344.94 mm^2, 2609.77 mm^2 and lowest surface area value of 2209.98 mm^2 respectively. The bottom surface and inner pores exhibited a golden-brown color indicating the occurrence of rust. The observed uniform corrosion occurs majorly because of oxidation. The low corrosion rate of the structures results from the chemistry of chromium oxide film formed on

the surface of the printed structures. The white interferometry imaging of the samples in Figure 18 shows that the samples morphology do not change even after corrosion.

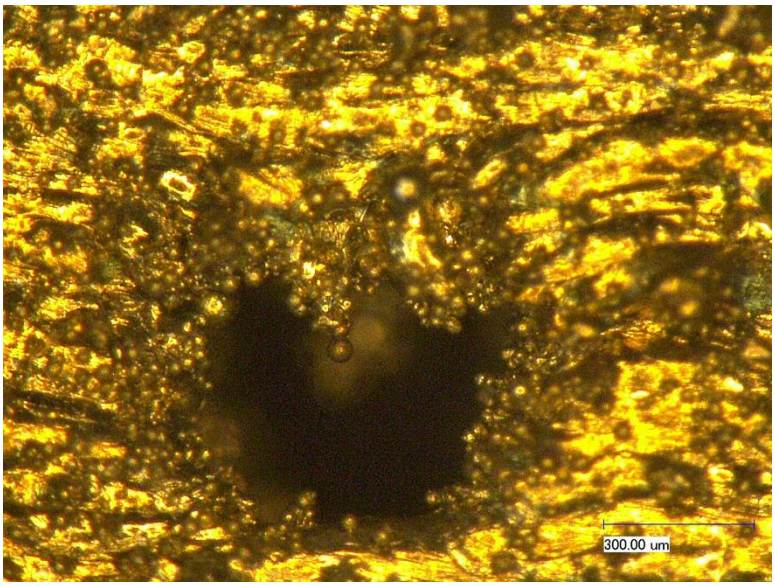

Figure 17. Optical micrograph of corrosion types on porous surface.

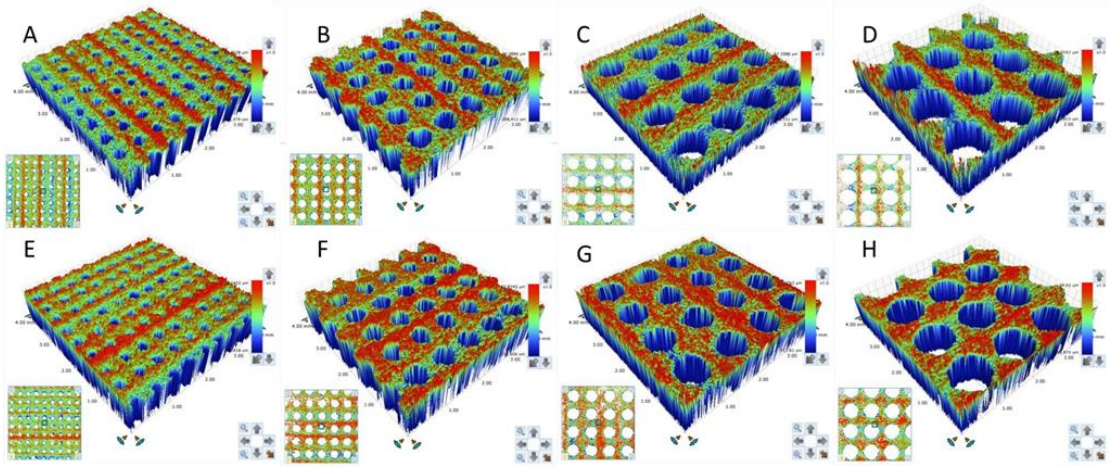

Figure 18. White interferometry of the 3D printed 316L porous structures (A) 0.4 mm (B) 0.6 mm (C) 0.8 mm (D) 1.0 mm, (E-H) Samples of A-D subjected to corrosion test.

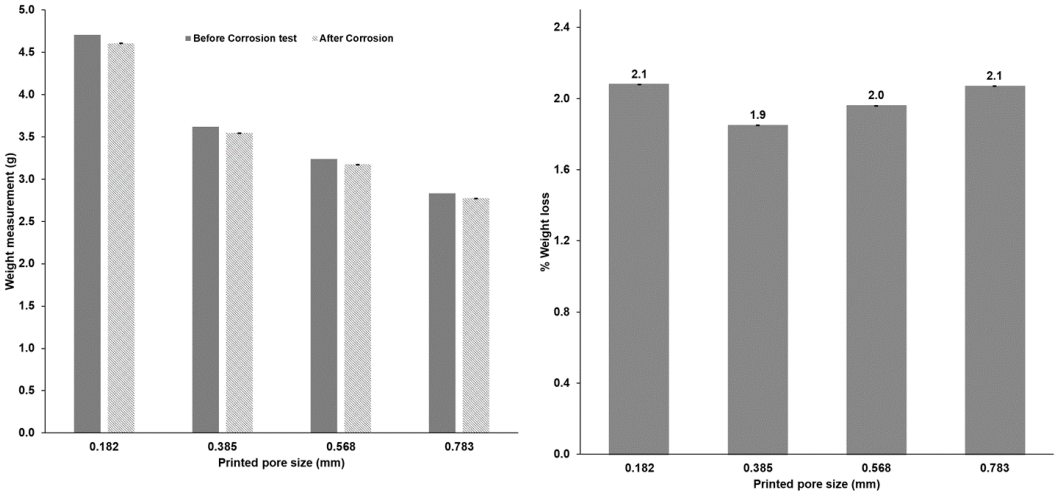

Figure 19. (a) Weight measurement of 3D printed samples; (b) Percentage weight loss due to corrosion test.

Table 7. Corrosion rate parameters for 336 hours in mpy

3d printed pore size	Weight loss (mg)	Surface Area (in^2)	Corrosion rate (mpy)
0.182	0.1	6.7	2.9
0.385	0.07	5.2	2.6
0.568	0.06	4.0	3.1
0.783	0.06	3.4	3.4

As the pore sizes increases, the percentage weight loss of the porous structures increases due to the increase in corrosion rate of the larger pore sizes, with an exception for the smallest pore size of 0.4 mm.

5.3 Effect of Pore size on Cell Adhesion via Cell Culture

Mean pore size constitutes a significant role on the scaffold's cell activity. The transfer of nutrients and waste products can be impeded if the pore size is small, resulting from the inability of the cells to move or grow in towards the center of the construct. Also, a large pore size can also limit Osseointegration of bones or cell attachment, as it may be too loose to be attached to the cell walls and may pass through the pores to the bottom of the wells [58, 61]. Hence the need to study and derive the optimal mean pore size that will support cell attachment, bone ingrowth, differentiation and cell proliferation. In addition to pore diameter, pore shape, porosity, surface area, and pore interconnectivity, play significant roles in enhancing the biological functions of the scaffolds [62-64]. In tissue engineering, scaffolds design should mimic the right tissues of the body, meeting the biological, geometrical and mechanical requirements [65]. Bone ingrowth allows cells to gain entry into the pores and move within the pores and be adhered onto the inner surfaces of the pore. Cells proliferation leads to the formation of new bone attached to the scaffold [66].

From the cell culture analysis, as shown in Figure 20, all pore sizes of the 316L stainless steel produced via SLM are biocompatible to support bacteria cell growth; We observed that the samples with the largest mean pore size 0.783 mm was most conducive for biofilm formation with a bacterial load of $170*10^3$ CFU/ml. The colony forming unit (CFU) of bacteria refers to a mass of individual cells of bacteria growing together. The CFU, obtained from plating the dislodged biofilm from each sample, represents the number of bacteria involved in the biofilm formation. The study samples of 0.182 mm, 0.385 mm, 0.568 mm, reveals cell growth of approximately $180*10^3$ CFU/ml, $13*10^3$ CFU/ml, and $76*10^3$ CFU/ml respectively.

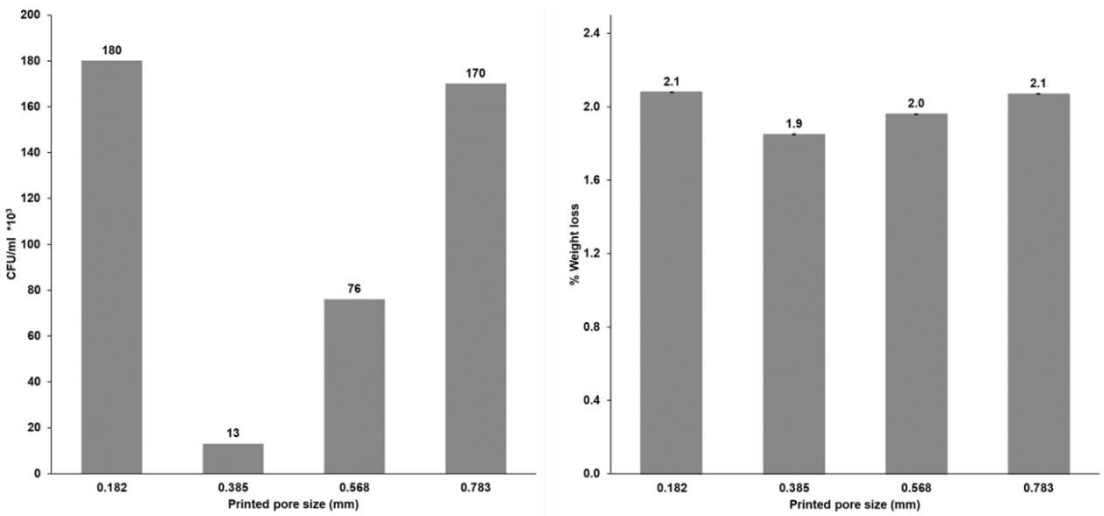

Figure 20. (a) Bacteria cell growth on 3D printed porous structures; (b) Percentage weight loss due to corrosion test.

The bacteria cells grown on the porous structures in Figure 21 appears as the whitish substances on the surface. Due to the balling effects on the morphology of the porous structures, the cells growth is quite challenging to read off from the SEM image, as the balling effect appears to resemble the cell growth (see Figure 21). The amount of biofilm formed reduces as the mean pore diameter decreases, the structures with printed pore sizes of 0.568 mm and 0.385 mm, both exhibited 2.2 and a 13-fold reduction in adhered bacteria respectively. An inconsistent trend of viable bacteria cells growth in CFU was observed, as a further decrease in pore size to 0.182 mm resulted in increased bacteria cell attachment, closely mimicking that of the largest pore size of 0.783 mm. The two highest amount of cell growth can be seen in the 0.182mm and 0.783 mm pore size samples of $180*10^3$ CFU/ml and $170*10^3$ CFU/ml respectively. The 0.385mm and the 0.568 mm pore size samples shows the least amount of bacterial cell growth, with a 95% confident that the values are valid, as the error bars for these samples do not overlap.

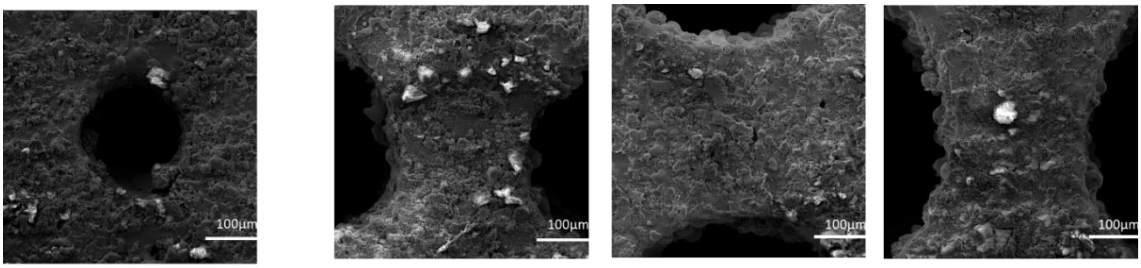

Figure 21. SEM image of bacteria cell growth on 3D printed porous structures.

Figure 20 shows that bacteria cell growth increases with an increase in pore size, with a deviation of the 0.182 mm mean pore size which recorded the greatest amount of cell growth in $180*10^3$ CFU/ml. Comparing the cell growth and percentage weight loss in Figure 20, a similar trend can be observed. The percentage weight loss also increases as the mean pore size increases with an exception for the 0.182 mm mean pore size of 2.18% weight loss. The 0.385 mm, 0.568 mm, and 0.783 mm possess a percentage weight loss of 1.85%, 1.96% and 2.07% respectively.

The 316L stainless steel material is biocompatible, serving as a good host for Pseudomonas aeruginosa bacteria cells. Based on various studies, the minimum pore size range for cell ingrowth ranges from 0.1 to 0.4 mm [65]. Another account records a minimum pore size of 0.05 mm to support bone ingrowth [66]. As earlier discussed in chapter 4, all the samples exhibited a pore size reduction of approximately 0.220 mm. The pores of the 0.4 mm porous sample, for instance, was reduced to 0.182 mm, with pores almost closed and non-uniformly rounded. It is quite challenging to fabricate uniform, and well-defined pore sizes less than 0.4 mm.

A tentative reason for the increase in bacteria cell growth for the smallest pore size, is owed to the fact that the smaller pore size promotes cell proliferation and cell adhesion on the surface but impedes cell ingrowth into the pores by completely overgrowing the pores or by the single cell

stretching across the pore width [66]. As the pore occlusion trend changes, when the pore size increase from 0.182 mm to 0.385 mm, more in-depth investigation may reveal that pore sizes less than 0.385 mm supports cell attachment, but beyond 0.385 mm, cell ingrowth begins to form. This term is referred to as pore overgrowth or pore occlusion. On the other hand, larger pore sizes of up to 1.0 mm, possess more open space for cell growth, enhance migration of cells into pores, as the rate of cell ingrowth increases with pore size.

The SLM technique supports cell functions on the porous structures. Direct laser forming (similar to SLM technique) [65] manufactured Ti6AL4V specimens with a pore size of 0.5 mm, supports overgrown osteoblast cells covering its pore surface, while the human osteoblast culture on the larger pore sizes of 0.7 mm and 1 mm did not completely overgrow the pores, but allowed cell ingrowth into the pore [67]. Pore over-growth in osteoblast is necessary for bone formation and osseointegration of the bone to the scaffolds, for permanent implants applications. If otherwise, then larger pores which possess lower pore-overgrowth is favorable, as the pore size of the external surface can be larger than the internal surface, which it surrounds, for cell movement through the outer surface into the interior surface and to enhance vascularization, which is necessary for bone tissue regeneration [67]. These characteristics promote oxygen and nutrient flow.

This research evaluates the feasibility and effects of pore architecture on supporting cell viability, adhesion, and growth. Functionally graded scaffolds have the potential of improving the quality of the scaffolds, as it incorporates the advantages of small pores (< 0.5mm) on the internal surface of the scaffold for initial cell adhesion and larger pores (>1 mm) on the external part of the scaffold to promote the supply of nutrients and oxygen and prevent occlusion [68]. Larger pore sizes increase permeability; in cases where low permeability is required to attain cell adhesion, the

pores can be reduced. A reduction in permeability improves the seeding efficiency [69]. SLM and other AM techniques offer the opportunity for various complex pore sizes and shapes in one structure meeting both mechanical and biological requirement [66]. Triangularly shaped pores support cell proliferation and differentiation but might impede or reduce the time of occurrence of pore occlusion [68]. A large surface area also promotes fixation of cells on the implant surface, in this research, the 0.182 mm sample possesses the largest surface area of 4305.73 mm^2, this may have accounted for the increase in the number of cell growth in CFU. Corners in scaffolds aids cell growth [66].

The roughness associated with the pore has an impact on cell growth. Further research will include characterizing the roughness of the samples and finding its correlation with the cell adhesion and growth pattern [66]. Pore architecture, spanning over pore shape, pore size, pore interconnectivity, porosity, can help in advancing additive manufactured customized parts for application in the biomedical field and tissue engineering. To determine the optimal pore architecture, there is a need to balances the trade-off between cell adhesion, cell proliferation, cell differentiation, permeability, vascularization and mechanical strength. Phenomenon such as fluid transport, oxidation raises more questions of their effect on the cell growth pattern observed in this study, for example, the percentage weight loss trend is like that of the cell growth in CFU values, for all pore sizes. Oxidation may be responsible for providing nutrients to enhance cell growth. These should be further investigated.

CHAPTER VI

CONCLUSION AND FUTURE RECOMMENDATIONS

6.1 Conclusion

This research studied the effects of additive manufacturing techniques, i.e. SLM method, on the pore geometry of 316L stainless steel material of designed pore sizes of 0.4 mm, 0.6 mm, 0.8 mm, and 1.0 mm, the biocompatibility of the 3D printed 316L stainless steel for cell growth, and the pore size effect on the biological performance of Pseudomonas aeruginosa cells implanted on selective laser-melted scaffold models.

The 316L stainless steel porous structures with fully interconnected pores (defined holes) were successfully fabricated, using the SLM process, underscoring SLM as an effective method in producing interconnected porous structures and in processing 316L stainless steel.

There was a pore size reduction of 0.22 mm for all samples, indicating a printing error of 0.22 mm for the SLM production method. Also, as the pore sizes increase, the pores become well defined and regular in shape due to an increases pore spacing, a uniform pore distribution is achieved and porosity increases.

Improving the 3D printing process parameters will enhance the pore architecture. If the processing parameters of SLM manufacturing process for this research will be replicated for another study, then the minimum pore size that will be designed should be greater than 0.22 mm, to take into account, the printing error of 0.22 mm. As discussed earlier, pore architecture plays a vital role in improving cell performance and enhancing the mechanical properties of the scaffolds.

The cell culture of *Pseudomonas aeruginosa* on the 3D printed scaffold models reveals the cell growth viability of all samples of the 316L stainless steel material for pores size ranging from

0.182 mm to 0.783 mm. The 0.783 porous structure, with the highest porosity of 61.2%, was most conducive to biofilm formation, allowing cell ingrowth into the pores. The 0.182 mm smaller pore size aided cell adhesion and proliferation but limits the amount of cell ingrowth into the pores.

Three-D (3D) printed 316L stainless steel is a modeling system for biomaterials. From the results derived from this research, SLM processing of 316L stainless steel can be used to produce complex structures not easily achieved by traditional manufacturing methods, with high porosity level and cell growth viability. This research provides room for further research to determine the optimal structure and pore architecture design for enhancing cell performance and mechanical properties matching that of the human body, and that is customizable, based on a patient's anatomical data and needs, utilizing the advantages of 3D printing in manufacturing components from their CAD models.

6.2 Future Recommendations

Based on the findings on this research, suggestions are stated below to derive a generally accepted optimal scaffold design for cell viability, improved mechanical properties, that meet the biological and mechanical properties of the human body, as there are many optimal pore size variations:

1. Investigate the relationship between corrosion rate, oxidation on cell growth pattern and the amount in CFU, to understand the effect of oxidation and other underlying factors related to corrosion on cell proliferation.
2. Quantitative evaluation of the roughness of the porous structures and how they affect the cell growth, as this will aid in understanding the degree of roughness required in scaffold design for bone ingrowth. As previous research studies have shown that roughness provides a thriving ground for cell adhesion.
3. SLM printing process parameters should be varied, in other to study their effect in achieving well-defined structures, uniform pore distribution, as the CAD models. Samples fabricated based on varying printing process parameters, should be subjected to a biocompatibility test, to determine the optimal structural design for enhanced cell performance.
4. Investigation of the mechanical properties of the SLM printed 316L stainless steel structures, analyzed for biocompatibility and cell functionality performance, to determine and improve the overall performance of the scaffold, as there's a trade-off between cell adhesion, visualization, mechanical strength, permeability, etc., i.e., a high porosity, reduces the mechanical strength of the structure. A balance in the trade-off has a huge impact in optimizing scaffolds to meet the body requirements.

REFERENCES

1. Prinz, F.B., et al., *Rapid prototyping in Europe and Japan.* Center for Advanced Technology, 1997. **102**.
2. Wong, K.V. and A. Hernandez, *A review of additive manufacturing.* ISRN Mechanical Engineering, 2012. **2012**.
3. Horn, T.J. and O.L. Harrysson, *Overview of current additive manufacturing technologies and selected applications.* Science progress, 2012. **95**(3): p. 255-282.
4. Murr, L.E., et al., *Metal fabrication by additive manufacturing using laser and electron beam melting technologies.* Journal of Materials Science & Technology, 2012. **28**(1): p. 1-14.
5. Ryan, G., A. Pandit, and D.P. Apatsidis, *Fabrication methods of porous metals for use in orthopaedic applications.* Biomaterials, 2006. **27**(13): p. 2651-2670.
6. Li, X., et al., *Fabrication and characterization of porous Ti6Al4V parts for biomedical applications using electron beam melting process.* Materials Letters, 2009. **63**(3): p. 403-405.
7. Conner, B.P., et al., *Making sense of 3-D printing: Creating a map of additive manufacturing products and services.* Additive Manufacturing, 2014. **1**: p. 64-76.
8. Wohlers, T., *Direct digital manufacturing.* Manufacturing Engineering, 2009, January. **142**(1): p. 73-77,79-81.
9. Thomson Reuters. *Printed titanium parts expected to save millions in Boeing Dreamliner costs*. 2017, April 10; Available from https://www.reuters.com/article/us-norsk-

boeing/printed-titanium-parts-expected-to-save-millions-in-boeing-dreamliner-costs-idUSKBN17C264.

10. Verge, T. *3d-printed titanium parts could save Boeing up to $3 million per plane*, 2017, April 11; Available from https://www.theverge.com/2017/4/11/15256008/3d-printed-titanium-parts-boeing-dreamliner-787.

11. Levy, G.N., R. Schindel, and J.P. Kruth, *RAPID MANUFACTURING AND RAPID TOOLING WITH LAYER MANUFACTURING (LM) TECHNOLOGIES, STATE OF THE ART AND FUTURE PERSPECTIVES.* CIRP Annals, 2003. **52**(2): p. 589-609.

12. Herderick, E.D., *Progress in additive manufacturing.* JOM, 2015. **67**(3): p. 580-581.

13. Campbell, I., D. Bourell, and I. Gibson, *Additive manufacturing: rapid prototyping comes of age.* Rapid prototyping journal, 2012. **18**(4): p. 255-258.

14. Gao, W., et al., *The status, challenges, and future of additive manufacturing in engineering.* Computer-Aided Design, 2015. **69**: p. 65-89.

15. Swaelens, B., J. Pauwels, and W. Vancraen. *Support generation for rapid prototyping*. in *Proceedings of the Sixth International Conference on Rapid Prototyping*. 1995. University of Dayton, June.

16. Melchels, F.P., et al., *Additive manufacturing of tissues and organs.* Progress in Polymer Science, 2012. **37**(8): p. 1079-1104.

17. Meijer, G.J., et al., *Cell-based bone tissue engineering.* PLoS medicine, 2007. **4**(2): p. e9.

18. Seitz, H., et al., *Three‐dimensional printing of porous ceramic scaffolds for bone tissue engineering.* Journal of Biomedical Materials Research Part B: Applied Biomaterials, 2005. **74**(2): p. 782-788.

19. Rezwan, K., et al., *Biodegradable and bioactive porous polymer/inorganic composite scaffolds for bone tissue engineering.* Biomaterials, 2006. **27**(18): p. 3413-3431.

20. Hutmacher, D.W., *Scaffolds in tissue engineering bone and cartilage*, in *The Biomaterials: Silver Jubilee Compendium*. 2006, Elsevier. p. 175-189.

21. Loh, Q.L. and C. Choong, *Three-dimensional scaffolds for tissue engineering applications: role of porosity and pore size.* Tissue Engineering Part B: Reviews, 2013. **19**(6): p. 485-502.

22. Jones, A.C., et al., *The correlation of pore morphology, interconnectivity and physical properties of 3D ceramic scaffolds with bone ingrowth.* Biomaterials, 2009. **30**(7): p. 1440-1451.

23. Grayson, W.L., et al., *Biomimetic approach to tissue engineering.* Seminars in Cell & Developmental Biology, 2009. **20**(6): p. 665-673.

24. Causa, F., P.A. Netti, and L. Ambrosio, *A multi-functional scaffold for tissue regeneration: The need to engineer a tissue analogue.* Biomaterials, 2007. **28**(34): p. 5093-5099.

25. Nair, L.S. and C.T. Laurencin, *Polymers as Biomaterials for Tissue Engineering and Controlled Drug Delivery*, in *Tissue Engineering I*, K. Lee and D. Kaplan, Editors. 2006, Springer Berlin Heidelberg: Berlin, Heidelberg. p. 47-90.

26. Ryan, G.E., A.S. Pandit, and D.P. Apatsidis, *Porous titanium scaffolds fabricated using a rapid prototyping and powder metallurgy technique.* Biomaterials, 2008. **29**(27): p. 3625-3635.

27. Robertson, D.M., L. St Pierre, and R. Chahal, *Preliminary observations of bone ingrowth into porous materials.* Journal of Biomedical Materials Research Part A, 1976. **10**(3): p. 335-344.

28. Harte, A.M., N.A. Fleck, and M.F. Ashby, *Fatigue failure of an open cell and a closed cell aluminium alloy foam.* Acta Materialia, 1999. **47**(8): p. 2511-2524.

29. Körner, C. and R.F. Singer, *Processing of metal foams—challenges and opportunities.* Advanced Engineering Materials, 2000. **2**(4): p. 159-165.

30. Yamada, Y., et al., *Effects of heat treatment on compressive properties of AZ91 Mg and SG91A Al foams with open-cell structure.* Materials Science and Engineering: A, 2000. **280**(1): p. 225-228.

31. Jiang, B., et al., *A novel method for making open cell aluminum foams by powder sintering process.* Materials Letters, 2005. **59**(26): p. 3333-3336.

32. Singh, N.P., et al., *Aluminum syntactic foams ALFA for automotive applications.* Journal of KONES Internal Combustion Engines, 2003. **10**: p. 3-4.

33. Fauchais, P., *Understanding plasma spraying.* Journal of Physics D: Applied Physics, 2004. **37**(9): p. R86.

34. Kruth, J.-P., M.-C. Leu, and T. Nakagawa, *Progress in additive manufacturing and rapid prototyping.* Cirp Annals, 1998. **47**(2): p. 525-540.

35. Kruth, J.-P., *Material incress manufacturing by rapid prototyping techniques.* CIRP Annals-Manufacturing Technology, 1991. **40**(2): p. 603-614.

36. Mueller, B., *Additive manufacturing technologies–Rapid prototyping to direct digital manufacturing.* Assembly Automation, 2012. **32**(2).

37. Kruth, J.-P., et al., *Selective laser melting of iron-based powder.* Journal of materials processing technology, 2004. **149**(1-3): p. 616-622.

38. Hofmeister, W., et al., *Investigating solidification with the laser-engineered net shaping (LENSTM) process.* JOM, 1999. **51**(7): p. 1-6.

39. Atwood, C., et al., *Laser engineered net shaping (LENS (TM)): A tool for direct fabrication of metal parts*. 1998, Sandia National Laboratories, Albuquerque, NM, and Livermore, CA.

40. Mudge, R.P. and N.R. Wald, *Laser engineered net shaping advances additive manufacturing and repair.* Welding Journal-New York-, 2007. **86**(1): p. 44.

41. Liu, W. and J.N. DuPont, *Fabrication of functionally graded TiC/Ti composites by Laser Engineered Net Shaping.* Scripta Materialia, 2003. **48**(9): p. 1337-1342.

42. O'Brien, F.J., *Biomaterials & scaffolds for tissue engineering.* Materials Today, 2011. **14**(3): p. 88-95.

43. Nasab, M.B., M.R. Hassan, and B.B. Sahari, *Metallic biomaterials of knee and hip-A review.* Trends Biomater. Artif. Organs, 2010. **24**(1): p. 69-82.

44. Singh, R. and N.B. Dahotre, *Corrosion degradation and prevention by surface modification of biometallic materials.* Journal of Materials Science: Materials in Medicine, 2007. **18**(5): p. 725-751.

45. Alvarado, J., et al., *Biomechanics of hip and knee prostheses.* Applications of Engineering Mechanics in Medicine, GED–University of Puerto Rico Mayaguez, 2003.

46. Ramsden, J.J., et al., *The design and manufacture of biomedical surfaces.* CIRP Annals-Manufacturing Technology, 2007. **56**(2): p. 687-711.

47. Park, B. and Y.K. Kim, *Metallic biomaterials.* Balance, 2003. **1**: p. 50.

48. Ambrosio, A., et al., *A novel amorphous calcium phosphate polymer ceramic for bone repair: I. Synthesis and characterization.* Journal of Biomedical Materials Research Part A, 2001. **58**(3): p. 295-301.

49. PENN STAINLESS PRODUCT, I. *Stainless grades*. 2013, July 29; Available from: http://www.pennstainless.com/.

50. Sing, S.L., et al., *Laser and electron‐beam powder‐bed additive manufacturing of metallic implants: A review on processes, materials and designs.* Journal of Orthopaedic Research, 2016. **34**(3): p. 369-385.

51. Ozdemir, O., et al., *An investigation on boriding kinetics of AISI 316 stainless steel.* Vacuum, 2008. **83**(1): p. 175-179.

52. *SS 317L-0407 powder for additive manufacturing*. renishaw.com, 2015.

53. Gu, D., et al., *Laser additive manufacturing of metallic components: materials, processes and mechanisms.* International materials reviews, 2012. **57**(3): p. 133-164.

54. Mechanical Engineering, T.A.M.U. *VEGA II LSU SEM*. 2017 [cited 2018, May 16; Available from: https://engineering.tamu.edu/mechanical/facility-services/shared-services-facility.html.

55. Fontana, M.G., *Corrosion Engineering*. 1987: McGraw Hill.

56. Souness, A., et al., *Influence of scaffold design on 3D printed cell constructs.* Journal of Biomedical Materials Research Part B: Applied Biomaterials, 2017.

57. Kusuma, C., et al., *Effect of Laser Power and Scan Speed on Melt Pool Characteristics of Commercially Pure Titanium (CP-Ti).* Journal of Materials Engineering and Performance, 2017. **26**(7): p. 3560-3568.

58. Čapek, J., et al., *Highly porous, low elastic modulus 316L stainless steel scaffold prepared by selective laser melting.* Materials Science and Engineering: C, 2016. **69**: p. 631-639.

59. Harun, W.S.W., et al., *A review of powdered additive manufacturing techniques for Ti-6al-4v biomedical applications.* Powder Technology, 2018. **331**: p. 74-97.

60. Li, R., et al., *316L stainless steel with gradient porosity fabricated by selective laser melting.* Journal of Materials Engineering and Performance, 2010. **19**(5): p. 666-671.

61. Murphy, C.M. and F.J. O'Brien, *Understanding the effect of mean pore size on cell activity in collagen-glycosaminoglycan scaffolds.* Cell adhesion & migration, 2010. **4**(3): p. 377-381.

62. Leong, K., C. Cheah, and C. Chua, *Solid freeform fabrication of three-dimensional scaffolds for engineering replacement tissues and organs.* Biomaterials, 2003. **24**(13): p. 2363-2378.

63. Karageorgiou, V. and D. Kaplan, *Porosity of 3D biomaterial scaffolds and osteogenesis.* Biomaterials, 2005. **26**(27): p. 5474-5491.

64. Hollister, S.J., *Scaffold engineering: a bridge to where?* Biofabrication, 2009. **1**(1): p. 012001.

65. Warnke, P.H., et al., *Rapid prototyping: porous titanium alloy scaffolds produced by selective laser melting for bone tissue engineering.* Tissue engineering part c: Methods, 2008. **15**(2): p. 115-124.

66. Tan, X.P., et al., *Metallic powder-bed based 3D printing of cellular scaffolds for orthopaedic implants: A state-of-the-art review on manufacturing, topological design,*

mechanical properties and biocompatibility. Materials Science and Engineering: C, 2017. **76**: p. 1328-1343.

67. Hollander, D.A., et al., *Structural, mechanical and in vitro characterization of individually structured Ti–6Al–4V produced by direct laser forming.* Biomaterials, 2006. **27**(7): p. 955-963.

68. Van Bael, S., et al., *The effect of pore geometry on the in vitro biological behavior of human periosteum-derived cells seeded on selective laser-melted Ti6Al4V bone scaffolds.* Acta Biomaterialia, 2012. **8**(7): p. 2824-2834.

69. Impens, S., et al., *Controlled cell-seeding methodologies: a first step toward clinically relevant bone tissue engineering strategies.* Tissue Engineering Part C: Methods, 2010. **16**(6): p. 1575-1583.